IEEE Access
Multidisciplinary ⋮ Rapid Review ⋮ Open Access Journal

Received 26 April 2024, accepted 12 May 2024, date of publication 16 May 2024, date of current version 28 May 2024.

Digital Object Identifier 10.1109/ACCESS.2024.3402082

RESEARCH ARTICLE

Co-Designing Wireless Networked Control Systems on IEEE 802.15.4-Based Links Under Wi-Fi Interference

YURIY ZACCHIA LUN[1], (Member, IEEE), CLAUDIA RINALDI[1,2], (Member, IEEE), ALESSANDRO D'INNOCENZO[1], (Member, IEEE), AND FORTUNATO SANTUCCI[1], (Senior Member, IEEE)

[1]Department of Information Engineering, Computer Science and Mathematics, University of L'Aquila, 67100 L'Aquila, Italy
[2]L'Aquila Research Unit, National Inter-University Consortium for Telecommunications (CNIT), 67100 L'Aquila, Italy

Corresponding author: Yuriy Zacchia Lun (yuriy.zacchialun@univaq.it)

This work was supported in part by the Italian Government through the National Operational Programme (NOP) on Research and Innovation 2014–2020, Inter-ministerial Committee for Economic Planning (CIPE) under Resolution 70/2017; in part by the Ministry for Universities and Research (MUR) National Recovery and Resilience Plan (NRRP) funded by the NextGenerationEU under Attraction and International Mobility (AIM) under Grant 1877124 (Activity 1); in part by the Centre of Excellence on Connected, Geo- Localized and Cybersecure Vehicles (EX-Emerge) Grant, and National Research Centre for High-Performance Computing, Big Data and Quantum Computing (ICSC) under Grant CN00000013; in part by the National Innovation Ecosystem Grant ECS00000041; and in part by the European Union through DigInTraCE and Resilient Trust under Grant GA 101091801 and Grant GA 1011112282.

ABSTRACT This paper proposes an analytical framework for co-designing wireless networked control systems (WNCSs) demonstrated in an industrial scenario. The framework allows us to quantitatively characterize the impact of wireless channel model accuracy when designing a controller to stabilize a WNCS. We consider a scenario consisting of two co-located wireless networks: the first connects the plant automation network backbone to field devices via WirelessHART, ISA-100.11a, or IEEE 802.15.4e, and the second uses IEEE 802.11 equipment to supply real-time multimedia data to the supervisory devices. First, we derive a parametric 802.11 interference characterization for an arbitrary number of active interfering devices and perform extensive parametric analysis. We then derive the message and packet error probability expressions necessary to develop an appropriate finite-state Markov channel model. Finally, we ran sizeable Monte Carlo simulations to evaluate the impact of our channel model on the control performance of a wireless closed-loop system and compared it with the performance obtained using a Bernoulli channel model.

INDEX TERMS Networked control systems, system analysis and design, wireless communication.

I. INTRODUCTION

The industrial Internet of Things (IIoT) is a fundamental pillar of digital manufacturing that connects all industrial assets, including industrial machinery and control systems, with information systems and business processes. It allows for collecting and analyzing large amounts of real-time data for optimal industrial operations [1]. Typical application scenarios include smart logistics, remote maintenance, and automated monitoring, control, and management [2]. In addition to manufacturing, IIoT has applications in building and process automation, intelligent transportation, precision agriculture, and smart grids [1], [3]. In contrast to the consumer Internet of Things (IoT), IIoT focuses on automation in industrial environments, involving hundreds to thousands of industrial assets (such as sensors, actuators, controllers, and other safety- and mission-critical industrial equipment), and presents stringent requirements on reliability, latency, energy efficiency, cost, interoperability, coexistence, security, and privacy [1], [2], [3].

This study addresses the reliability and coexistence requirements for one of the most essential IIoT applications: industrial control [4], [5], [6]. Wireless networked control systems (WNCSs) represent a key technical solution for the flexible deployment of industrial control, in which spatially distributed sensors, actuators, and controllers communicate

The associate editor coordinating the review of this manuscript and approving it for publication was Ronald Chang.

through wireless networks to observe and regulate the dynamics of physical plants [3], [6], [7]. Introducing a wireless communication method to replace reliable yet expensive and inflexible cable connections requires special care to guarantee control application-level requirements such as reliability and stability. Generally, it requires a challenging co-design process, particularly for industrial automation, in which the deployment stage is governed by stringent regulations that limit possible corrections and changes to an operational system. This aspect has attracted interest in exploiting realistic computational models in general scenarios, adhering to the actual behavior of a complex system. Indeed, the availability of detailed models enables the pursuit of application-level requirements during the design and simulation phases.

A proper cyber-physical co-design approach must melt and harmonize wireless models and control algorithms despite the many actors involved [8]. From a communication point of view, wireless channels dynamically vary in an industrial environment owing to moving obstacles, interference, temperature, and humidity. From a control perspective, the latency requirement of a plant is extremely stringent and challenging under randomly varying conditions [8]. For WNCSs, a survey [7] identified four critical variables that create interactions between WNCS control and communication subsystems: sampling period, message dropout and delay, and network energy consumption. This paper focuses on message dropouts, whose accurate probability derivation is fundamental for successfully implementing interactive and joint WNCS design approaches. The leading causes of message dropout are symbol errors and packet losses resulting from complex interactions. In WNCSs, messages carry sensor samples to controllers or control commands to actuators, that is, protocol data units (PDUs) in the control application layer. Communication protocols convert messages to lower-layer PDUs, which become network packets at the network layer, frames at the data link layer, and physical layer PDUs (PPDUs), also called physical layer (PHY) packets [9], at the lowest layer. Network congestion leads to network packet losses, whereas radio channel impairment and interference cause symbol errors, resulting in PPDU corruption. Therefore, a WNCS designer must consider the contributions of various protocol layers to the dropout probability of an application message, with the awareness that neglecting the bursty nature of communication errors in a wireless networked environment may lead to control system performance degradation and even stability loss. Indeed, in [10], the authors showed that the Bernoulli packet loss model, extensively used by the control theory scientific community, is incapable of capturing the loss of stability due to bursts of packet losses. In contrast, a Markov packet loss model can adequately address stability issues. The focus of this paper is to formally characterize the impact of channel model accuracy when designing a controller to stabilize a WNCS in an industrial scenario. It addresses two co-located wireless networks. The first connects the plant automation network backbone to field devices via WirelessHART, ISA-100.11a, or IEEE 802.15.4e. The second wireless network uses IEEE 802.11 equipment to supply real-time multimedia data to the supervisory devices [11]. Section II provides a detailed description of the reference scenario used to examine the worst-case interference environment for the coexistence analysis.

A. CONTRIBUTIONS

This paper presents a comprehensive analytical framework for co-designing delay-sensitive WNCSs with message dropouts. We validate the application of the framework to an industrial scenario that requires the coexistence of different wireless networks through sizable Monte Carlo simulations. The main contributions of this study are as follows:

- We introduce a comprehensive analytical co-design framework for WNCSs subject to message dropouts that relies on a four-step procedure that produces accurate stochastic finite-state link abstractions and allows precise end-to-end message loss modeling.
- We demonstrate the framework in an industrial setting of IEEE 802.15.4 and 802.11 networks coexisting at the same site. In doing so, we derive a novel parametric 802.11 interference characterization for an arbitrary number of active interfering devices affecting the reference user and message and packet error probability expressions considering the chip sequence structure of 802.15.4 symbols.
- We provide an extensive parametric analysis of the derived interference power spectral density (PSD), PHY packet corruption probability, and their impact on wireless feedback control performance in terms of the mean-square stability and control cost.

B. ORGANIZATION

The remainder of this paper is organized as follows. Section II presents a reference scenario that provides a concrete example of communication in an industrial setting using wireless feedback control. Section III examines the state-of-the-art related to analytical link characterization in industrial networks and wireless networked control systems coupled design. Section IV explores the interplay between the communication and control subsystems that affect message dropouts in wireless communication. Section V presents the first main contribution of the study, the analytical co-design framework, and the following sections illustrate this framework in the reference scenario. Section VI outlines the relevant transmitted signals, channel impairments, and receivers. Section VII provides the second main contribution, IEEE 802.11 parametric interference characterization, and Section VIII describes the general approach to message error probability derivation and analytical expressions for the reference scenario as another contribution. Section IX presents the derivation of the stochastic finite-state link model and the quality metrics to select the appropriate model parameters. Section X outlines the wireless control system architecture considering stochastic message loss and mean square stability. Finally, Section XI examines the impact of the interfering network on wireless networked control performance in terms of closed-loop stability and control cost. Section XII presents our final remarks and conclusions.

II. SCENARIO

The reference scenario considers two wireless networks operating in the 2.4 GHz industrial, scientific, and medical (ISM) radio band at the same industrial site. The first wireless network connects the plant automation network backbone to field devices using the WirelessHART, ISA-100.11a, or IEEE 802.15.4e communication standards. The second wireless network uses IEEE 802.11 equipment to supply real-time multimedia data to supervisory devices [11], [12]. We focus on the first wireless network that relies on one of the most adopted communication standards for WNCSs, IEEE 802.15.4 [9], considering some enhancements adopted by WirelessHART, ISA-100.11a, and IEEE 802.15.4e. Specifically, these three industrial wireless communication standards use the physical layer of IEEE 802.15.4 with additional time division multiple access (TDMA), frequency hopping, and multipath routing features to improve the timeliness and reliability of message delivery and lower energy consumption [7]. Point-to-point communication that belongs to the second wireless network interferes with the single-hop link of interest (LoI) within the first network. Fig. 1 shows this scenario, where the reference user is a field device at the center of the figure. Notably, the wireless network architecture depicted in Fig. 1 is fully compatible with WirelessHART and ISA-100.11a standards. Furthermore, having the reference user directly connected to the access point is consistent with the star topology required by the low-latency deterministic network (LLDN) mode in IEEE 802.15.4e. The LoI uses IEEE 802.15.4 guaranteed timeslots (GTSs) to deliver periodic (time-triggered) sensor measurements or control commands and thus does not rely on carrier-sense multiple access with collision avoidance (CSMA/CA) [9, pp. 113–114]. If the optional clear channel assessment (CCA) mechanism is enabled, we assume that it operates in Mode 2: carrier sense only [9, p. 457], meaning that the first network devices are hidden from the IEEE 802.11 stations and vice versa. This assumption, which is also used, for instance, in [13] and [14], allows us to examine the worst-case interference environment. Furthermore, we assume that the IEEE 802.11 network operates in a saturated condition modeled as in [15] and formally described in Section VII to analyze the worst interference case. For the coexistence analysis of IEEE 802.15.4 and 802.11 in different contention-based channel access settings without considering the communication and control coupled design, see, for example, [16] and [17], and references therein.

We remark that the presented scenario, with the communication protocols involved and the control problem, belongs to the IIoT use cases requiring stringent reliability, low latency, and, thus, limited interference [18]. Consequently, we are dealing with a WNCS for IIoT [3].

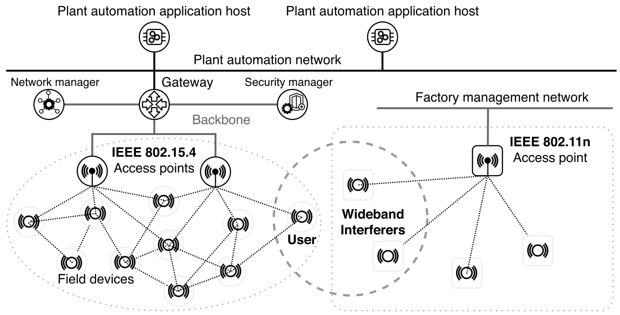

FIGURE 1. Different wireless networks located at the same industrial site.

III. RELATED WORKS

A. ANALYTICAL LINK MODELING

Analytical models of wireless channels are fundamental for a proper coupled design approach and for studying the behavior of this type of communication prior to deployment. Indeed, various studies on developing wireless link models are available in the literature. The industrial scenario in this paper considers communication protocols based on the physical and medium access control (MAC) layers of IEEE 802.15.4. Thus, we restrict our attention to analytical modeling for this specific standard. IEEE 802.15.4 contention-based MAC modeling is the focus of several studies (for instance, [19], [20], [21], and [22]). These studies do not consider IEEE 802.15.4 PHY and are complementary to the setting of this study, which takes advantage of the superframe contention-free period in the beacon-enabled mode. Other works, such as [23] and [24], capture both the PHY and MAC layer behaviors of IEEE 802.15.4 networks in the non-beacon-enabled mode. Focusing exclusively on PHY, [25] and [26] thoroughly analyzed concurrent transmissions with consequent packet collisions from co-channel interference. Notably, they neglected the effects of thermal noise and channel impairments, such as path loss, shadowing, and fading, to isolate the contribution of instantaneous interference power to the signal-to-interference ratio (SIR).

Various modeling studies have also examined interference from different communication standards to provide tools for coexistence analysis [1], [16], [17], [27], and [28]. Notably, the available analytical coexistence models represent interfering networks in saturated conditions [17], often in a particular setting, where each device within an interfering network is equidistant from the reference user and thus similarly affects the link of interest. For instance, [13] presented an interference model for co-located wireless networks using the IEEE 802.11b, Bluetooth, and ZigBee communication protocols. The reference user operating in the setting above is a ZigBee Coordinator (i.e., an access point based on IEEE 802.15.4) that sends data packets of one specific size according to the basic medium access mechanism, and the propagation environment accounts only for the path loss. In Section VII, we generalize the coexistence analysis to a setting with an application-dependent size of IEEE 802.15.4 data packets, different IEEE 802.11n medium access mechanisms, and a subset of interfering devices affecting the link of interest (instead of assuming that every Wi-Fi station in the network is in a position to create significant interference with the reference user). Furthermore, in Section VIII-C, we derive the first- and second-order packet error rate statistics by considering the receiver's thermal noise, channel impairments, and arbitrary positions of the interfering devices in the propagation environment. We rely on these statistics to find an adequate finite-state link model for a reliable WNCS co-design.

B. WNCSS CO-DESIGN

The main challenge of WNCS design is the tight interaction between the communication and control subsystems [7]. The survey [7] provides an extensive literature review of the mutual effects of these two subsystems on the overall system performance and interactive and joint design approaches for generic WNCSs. The review article [8] focuses on industrial applications, real-time scheduling algorithms, and cyber-physical co-design. The survey [29] addressed a smart manufacturing scenario presenting a WNCS architecture suitable for distributed control under Bernoulli packet loss approximation. This study presents a comprehensive analytical framework for co-designing generic delay-sensitive WNCSs, particularly suitable for industrial scenarios, showing when it is appropriate to rely on the Bernoulli packet loss assumption and when a more accurate finite-state Markov channel (FSMC) message loss model is necessary to guarantee a stable performance. The analytical results on the control and estimation of linear plants over lossy links that follow the Bernoulli distribution date back to the seminal paper [30], whereas the relevant results that consider the FSMC models are more recent [10], [31], [32]. The latest developments in WNCSs co-design range from transmission scheduling for remote state estimation and control under Bernoulli and FSMC packet dropouts [4], [33], [34], [35] to trade-offs in latency, reliability, data rate, and packet length [5], [6], [36] without forgetting security [37], [38], [39], [40], [41], communication quality of service [42], [43], coding-free transmissions [3], and predictive control [44], [45], [46], [47]. Notably, most studies rely on the Bernoulli packet loss model without specifying when it is appropriate, and they can benefit from the results of this study by selecting a suitable wireless link abstraction.

IV. THE INTERPLAY BETWEEN COMMUNICATION AND CONTROL IN WNCS MESSAGE DROPOUTS

A. CONTROL SYSTEM ASPECTS

Each controlled system, also known as a plant, typically handles continuous signals that require quantization and sampling for digital transmission over a wireless network. Furthermore, the received control commands must undergo digital-to-analog conversion (DAC) to become control input signals from the actuators. Fig. 2 summarizes the features

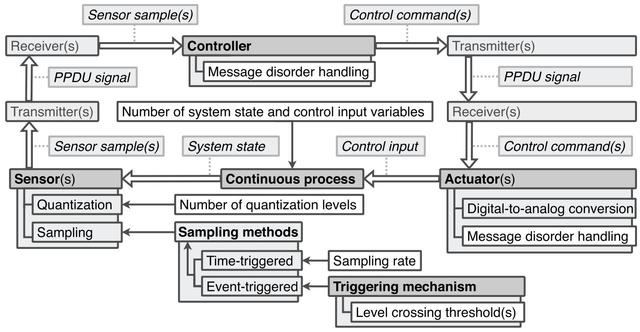

FIGURE 2. Control system features affecting message dropout process.

of these control systems that influence message dropouts in wireless communication. Depending on the system architecture, number of control inputs, and measured system state variables, several sensors and actuators interfacing with a continuous process may be connected to the same or different transceivers. The sensors measure the system state and perform sampling and quantization. The two main methods for sampling continuous-time signals are time-triggered and event-triggered sampling [7], [48]. Control system designers generally choose a sampling method and assign parameters based on the desired properties of a closed-loop system, including the response to reference signals and the impact of disturbances, network traffic, and computational load. Widely used time-triggered sampling generates regular periodic messages at fixed rates, allowing for precise scheduling of transmissions. In contrast to traditional digital control systems, where increasing the sampling frequency always translates to better performance, a higher sampling rate in WNCSs may result in performance degradation owing to network congestion [7]. Thus, for the time-triggered method, the sampling rate is a fundamental parameter that influences the network load and observable time correlations within fading-related channel impairments, as discussed in Section VIII-D. Event-triggered sampling aims to alleviate the traffic load by performing sensing and actuation only when the system requires attention owing to predetermined events, such as detecting or forecasting a significant degradation in stability or control performance, which creates an asynchronous traffic pattern and results in event-triggered or self-triggered control schemes, or a combination thereof [7]. These schemes comprise a feedback controller that computes the control commands, and a triggering mechanism that determines when to update the control input. Each choice of triggering mechanism and related level-crossing thresholds imposes a certain time lapse between activation instants, affecting the network traffic load and perceivable fading correlation. Quantization is also particularly relevant for WNCSs because the number of quantization levels shapes the size of the system input and output variables to be transmitted. The plant characteristics determine the number of variables. Consequently, quantization limits the size of the messages and thus impacts energy consumption and spectrum usage. As detailed in Section VIII, the message size also affects the PPDU size and the PHY packet loss probability. From an applicative point of view, floating-point quantization [49], used in digital signal processing and scientific computing is widespread in industrial automation [50], [51], whereas fixed-point quantization is attractive for embedded platforms [52]. Finally, the DAC of the control commands sent to the actuators may contribute to the message dropout process at the actuation link. Specifically, the popular logic zero-order hold (ZOH) signal reconstruction mechanism incorporates message disorder handling that keeps the newest message and discards the old ones based on their transmission time stamps [53]. A control algorithm may follow a similar logic by discarding disordered messages received from sensors when network-induced time delays cause some older data to arrive first. As detailed in the following subsection, message disorder is especially relevant in multi-hop wireless networks, presenting challenges to the control subsystem and the network itself [7].

B. COMMUNICATION ASPECTS

Several communication protocol layers contribute to the final message dropouts, with the lower layers treating PHY packet losses and the network layer determining network packet losses. Thus, we distinguished between lower- and network-level facets.

1) PHYSICAL AND DATA LINK LAYER CONSIDERATIONS

The physical layer transfers information across a communication network through a transmission medium, thereby conveying the energy of the signal from the transmitter to the receiver [54]. Specifically, the transmitter employs signal-processing techniques (such as modulation, spectrum spreading, and channel encoding) to convert messages into a form suitable for propagation through a physical channel. Common modulation methods used in current communication standards for WNCSs include minimum shift keying (MSK), offset quadrature phase-shift keying (OQPSK), binary phase-shift keying (BPSK), and variants of quadrature amplitude modulation (QAM) [9], [55]. Modulation techniques mediate the transmission rate, signal bandwidth, transmit power, symbol error rate (SER), and complexity. Spectrum spreading methods, such as the direct sequence spread spectrum (DSSS), frequency-hopping spread spectrum (FHSS), and chirp spread spectrum (CSS), trade a significant bandwidth increase for noise and interference reduction. DSSS relies on pseudo-random noise-like (PN) spreading sequences to encode PPDU data, whereas FHSS uses PN sequences to define channel-hopping. CSS, instead, does not employ PN coding, building on the linear characteristics of its frequency sweep signals, also known as chirps [9], [56]. As a part of the communication protocol, channel encoding introduces redundant data to detect and possibly correct channel-induced symbol errors. The significant channel coding parameters include the efficiency (overhead and induced delay), error control capability, and complexity [57].

Communication may also rely on diversity techniques to deliver several versions of the same message to improve the reliability of the data link [7]. Notably, multiple antennas enable space and angle diversity, whereas cross-polarized antennas allow polarization diversity [54]. The reduced message dropout probability comes at the cost of increased complexity and energy consumption. Time diversity primarily consists of retransmitting entire damaged packets or only corrupted data to recover the message content [58]. However, retransmission always requires repeated medium access and significantly increases the latency, rendering it unsuitable for delay-sensitive control applications. When implemented, retransmission relies on automatic repeat request (ARQ) error control strategies in their pure or hybrid forms [57].

MAC techniques affect both message delays and packet losses. Contention-based channel access protocols [7] mainly adopt the CSMA/CA mechanism to dispose centralized or distributed scheduling at the cost of random delay, additional packet loss to collisions, and possible channel congestion. Schedule-based access protocols, such as time-division multiple access (TDMA) and time-slotted channel hopping (TSCH), provide collision-free transmissions with deterministic guarantees on message delay but require efficient scheduling algorithms. Notably, TSCH divides the available bandwidth into separate non-overlapping frequency channels and relies on frequency-division multiple access (FDMA) to allocate each channel to a separate user in a given time slot. Transmitting subsequent packets on different channels increases link robustness to interference and channel impairments, as described in the following subsection [59]. The transmit power level of the transmitter is proportional to the signal-to-interference-plus-noise ratio (SINR) of the corresponding receiver. Higher SINR values ensure a lower SER for all the demodulation and decoding formats. However, increasing the transmit power at neighboring nodes may result in an interference power boost, which lowers the receiver SINR. Furthermore, increasing the transmit power translates into higher energy consumption. The data rate and PPDU size determine the transmission delay [7] and influence packet loss probability. A larger PHY packet size results in longer transmission delays and a higher likelihood of symbol errors, resulting in message dropout. Meanwhile, a higher data rate decreases the transmission delay, but this may not be achievable by some modulation and demodulation techniques. Thus, the data rate specifications dictate the choice of modulation and demodulation methods, resulting in specific SER values for each SINR.

Notably, modulation may allow for different demodulation approaches with various complexities, SER, and additional requirements for the received signals. For instance, a receiver can use coherent or non-coherent demodulation schemes to convert an MSK signal into corresponding data symbols [60], [61]. A coherent MSK demodulation has optimal SER performance but may require a complex design to address its susceptibility to the initial phase mismatch and residual carrier frequency offset. In contrast, non-coherent MSK

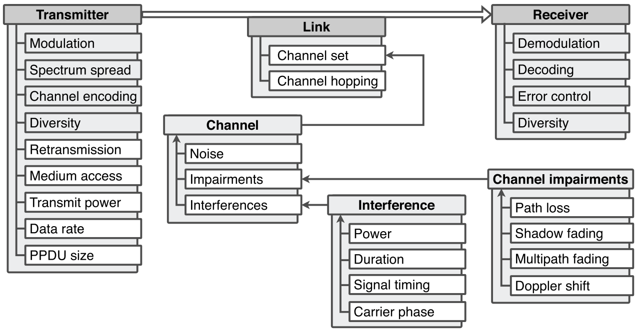

FIGURE 3. Wireless communication subsystem parameters and variables affecting symbol error ratio and probability of the physical layer packet loss.

demodulation approaches do not require phase and carrier frequency synchronization; thus, they are generally simpler to implement but have worse SER performance. The detectors used in the demodulation schemes produce quantized outputs fed to channel decoders by exploiting the available redundancy to correct channel disturbances. A channel decoder performs either hard or soft decisions based on the available quantization levels compared to the number of possible waveforms in the signal alphabet. Notably, soft-decision decoding algorithms offer better SER performance at the cost of higher complexity and find prominent applications in digital communications over fading channels [57], [62].

2) MULTI-HOP NETWORK FEATURES

When control applications rely on multi-hop wireless networks, network packet losses and the discarding of disordered messages add to the message dropouts induced by the physical and data link layers. The PHY packet loss process affected by the communication subsystem aspects in Fig. 3 concerns single-hop links and is independent of network-induced losses. Extending a single-hop message dropout model to a multi-hop setting requires explicitly considering the network topology, routing protocol, and heterogeneous traffic load [7], [20]. Network traffic forwarded to and from neighboring nodes in a routing path adds to the traffic primarily generated by nodes performing sensing or control actions. The aggregated traffic load of each node determines the possibility of congestion-induced buffer overflow, which results in a network packet loss on a related route. When routing protocols allow for alternative or redundant routes, the destination may receive disordered messages owing to the different end-to-end delays on distinct paths. Subsequently, message disorder-handling mechanisms that discard outdated messages add to the overall message dropout rate. Similarly, a time-to-live (TTL) mechanism that limits the lifespan of network packets discards messages with excessive delay instead of forwarding them to a destination, thereby contributing to message dropout on the affected path. Finally, routing protocols that provide multiple redundant paths trade the improvement in end-to-end communication reliability with higher energy consumption, computational complexity, and network traffic load.

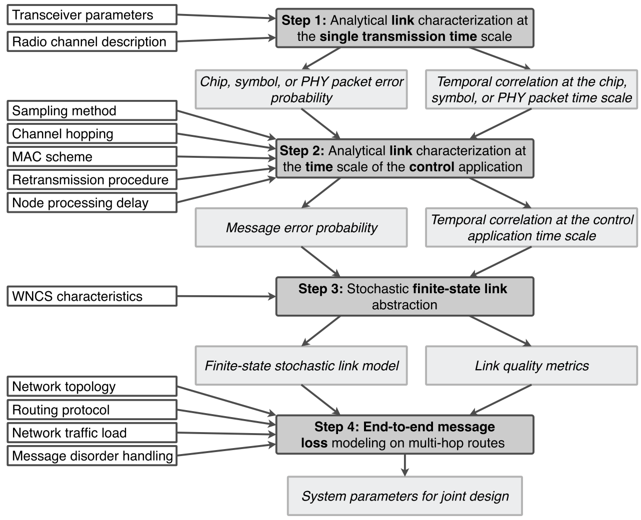

FIGURE 4. A four-step procedure implementing the analytical framework.

V. CO-DESIGN FRAMEWORK

This section presents our comprehensive analytical framework for co-designing delay-sensitive WNCSs based on the message dropout dependency analysis in the previous section and follows the bottom-up modeling approach articulated in the four main steps illustrated in Fig. 4. The first step accounts for the transceiver and propagation environment characteristics listed in Fig. 3 to describe the link temporal correlation properties at the transmission time scale and the related chip, symbol, or packet error probabilities. One can obtain the description of each radio link experimentally, from an extensive measurement campaign at an existing industrial site, or analytically by considering the geometry of the (actual or possible) propagation environment, the degree of motion around the communicating nodes, and the relevant physical phenomena involved. We followed the latter approach because it is not restricted to any particular industrial site, enabling technological feasibility and robustness analyses before committing to time-consuming and expensive measurement campaigns. Furthermore, empirical data from any measurement campaign allows us to calibrate our theoretical model. Notably, depending on the coherence time of the communication channel, fading may affect the signal that carries the control application message uniformly so that the PHY packet time-scale representation is appropriate. By contrast, symbols or even single chips may experience different attenuations and phase changes in a fast-fading setting, requiring a more refined time-scale description. Then, based on the sampling method, channel-hopping sequence, MAC scheme, retransmission procedure, and transmitting node processing delay pattern, the second step of the framework estimates the number of communication channel state evolutions between two consecutive control-application-related data transmissions. This second step allows us to assess the temporal correlation of each link at the time scale of the control application and to choose the relevant stochastic model of the PHY packet loss in the third step. If consecutive transmissions are uncorrelated, the Bernoulli process is the correct choice. When there is a time correlation between radio link states, the FSMC model may represent a better choice. To assess whether the selected model introduces a degree of conservatism, we rely on link quality metrics such as the expected value and variance of the PHY packet loss process and the maximum number of consecutive dropouts. Furthermore, depending on the WNCS properties, such as strong controllability [10], a simpler stochastic model, such as the Bernoulli message dropout process, may still be perfectly applicable in a more complex FSMC setting. The fourth step extends the single-hop model to multi-hop scenarios by composing end-to-end routes from the selected nodes and links. The resulting end-to-end message loss modeling should consider the network topology and routing protocol, expected evolution of the traffic load, and selected message disorder-handling mechanism at the control application level, thereby producing a set of system parameters for joint communication and control design.

The following sections apply the co-design framework to the reference scenario in Section II. Sections VI and VII implement the first step in Fig. 4. Section VI derives the analytical link model for IEEE 802.15.4-compatible transceivers operating on wireless channels subject to impairments, additive white Gaussian noise (AWGN), and generic interference. Then, Section VII provides a detailed description of IEEE 802.11n interference. Sections VIII and IX implement the second and third steps in Fig. 4, providing all the necessary parameters for the joint design of communication and control in a WNCS operating on single-hop routes.

VI. ANALYTICAL LINK CHARACTERIZATION

This section investigates the main blocks of the communication chain from the 802.15.4 transmitter to the receiver from the reference scenario in Section II. Section VI-A describes the signals transmitted on the link of interest, Section VI-B characterizes the radio propagation scenario, and Section VI-C outlines the receiver model.

A. IEEE 802.15.4 SIGNAL FORMAT

This section explicitly accounts for the transmitter characteristics summarized in Fig. 3, and our focus is on delay-sensitive control applications supported by the first wireless network. Therefore, the baseline case considers single-antenna transceivers, TSCH MAC, and no time diversity in the form of retransmission. In this case study, the transmitted signals use offset quadrature phase-shift keying direct-sequence spread spectrum (OQPSK-DSSS) modulation with a half-sine pulse-shaping filter [63] required by the IEEE 802.15.4 2450 MHz DSSS PHY, which is common to all the considered industrial wireless communication standards.

We write the passband signal of interest (SoI) encoding a PPDU in its canonical form as

$$\mathcal{X}(t) = b_I(t)\varphi_I(t) - b_Q(t)\varphi_Q(t), \tag{1}$$

where $b_j(t)$ is the baseband data signal (BDS) on the in-phase (if $j = I$) or quadrature ($j = Q$) component of the signal and $\varphi_I(t)$ and $\varphi_Q(t)$ are the signal space basis functions for the minimum shift keying (MSK) modulation.

$$\begin{aligned}\varphi_I(t) &= \sqrt{\frac{2}{T_c}}\cos(\omega_c t)\cos(\omega_p t),\\ \varphi_Q(t) &= \sqrt{\frac{2}{T_c}}\sin(\omega_c t)\sin(\omega_p t).\end{aligned} \tag{2}$$

The factor ω_c in (2) is the carrier center angular frequency, $\omega_p \triangleq \pi/(2T_c)$ is the angular frequency of the baseband pulses, and T_c is the inverse of the chip rate (nominally 2.0 Mchip/s). Note that the MSK representation is equivalent to OQPSK with a half-sine pulse-shaping filter [62, p. 126]. A bi-dimensional constellation space implies that each chip sequence corresponding to a 4 bits symbol, as indicated in [9, p. 468], is split into two 16 chips sequences, where even-indexed chips are modulated onto the I-phase carrier, and odd-indexed chips are modulated onto the Q-phase one. This specification implies that any realization of a chip-level BDS before pulse shaping can be expressed as

$$\begin{aligned}b_I(t) &= \sum_{\ell=0}^{n_s-1}\sum_{m=0}^{15}\hat{b}_{I,\ell,m}\, h\left(\frac{t-2(m+16\ell)T_c}{2T_c}\right),\\ b_Q(t) &= \sum_{\ell=0}^{n_s-1}\sum_{m=0}^{15}\hat{b}_{Q,\ell,m}\, h\left(\frac{t-(2(m+16\ell)+1)T_c}{2T_c}\right).\end{aligned} \tag{3}$$

In (3), n_s is the number of 16-ary data symbols in the PPDU, $\hat{b}_{j,\ell,m}$ is a non-return-to-zero (NRZ) encoded value of the mth chip on the I or Q component of the pseudo-random noise (PN) sequence that encodes the ℓth symbol ($\hat{b}_{j,\ell,m} \in \{\pm 1\}\, \forall j, \ell, m$), and $h(t)$ is the rectangular pulse. In the following, we indicate by $\mathtt{S}_\mathtt{i}^\mathtt{I}$ and $\mathtt{S}_\mathtt{i}^\mathtt{Q}$ the in-phase and quadrature components of the symbol $\mathtt{i}$ waveform $\mathtt{S}_\mathtt{i}$, where $\mathtt{i}$ is a hexadecimal digit. Applying a half-sine pulse-shaping filter to $\mathtt{S}_\mathtt{i}^\mathtt{I}$ yields a waveform $\hat{\mathtt{S}}_\mathtt{i}^\mathtt{I}$, that is, $\hat{\mathtt{S}}_\mathtt{i}^\mathtt{I} = \mathtt{S}_\mathtt{i}^\mathtt{I}\cos(\omega_p t)$. Owing to the time offset between I and Q components, $\hat{\mathtt{S}}_\mathtt{i}^\mathtt{Q} = \mathtt{S}_\mathtt{i}^\mathtt{Q}\sin(\omega_p t)$. A concatenation of n_s signals, each of which is selected from $\{\mathtt{S}_\mathtt{i}^\mathtt{I}\}_{\mathtt{i}=0}^{\mathtt{F}}$, produces the BDS $b_I(t)$. Similarly, a sequence of n_s signals chosen from $\{\mathtt{S}_\mathtt{i}^\mathtt{Q}\}_{\mathtt{i}=0}^{\mathtt{F}}$ corresponds to the BDS $b_Q(t)$. Fig. 5 illustrates the encoding of octet 00111100 (3C in the hexadecimal (hex) notation) as an example of a chip-level BDS obtained from (3) with half-sine pulse shaping.

Let the ℓth segment of BDSs (3) encoding a symbol $\mathtt{s}$ be $\mathcal{S}_\ell \in \{\mathtt{S}_\mathtt{i}\}_{\mathtt{i}=0}^{\mathtt{F}}$. The related portion of the passband SoI is

$$\mathcal{X}_\ell = \mathcal{S}_\ell^I\varphi_I(t) - \mathcal{S}_\ell^Q\varphi_Q(t). \tag{4}$$

The hex values corresponding to the PN sequences defining the symbol-to-chip mapping specified by IEEE 802.15.4 for

TABLE 1. Symbol-to-chip mapping for the 2450 MHz DSSS PHY.

Symbol s	Chip values	Symbol s	Chip values
0	D9C3522E	8	8C96077B
1	EDDC3522	9	B8C96077
2	2ED9C352	A	7B8C9607
3	22ED9C35	B	77B8C960
4	522ED9C3	C	077B8C96
5	3522ED9C	D	6077B8C9
6	C3522ED9	E	96077B8C
7	9C3522ED	F	C96077B8

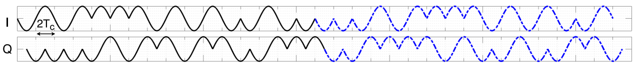

FIGURE 5. Sample baseband chip sequences with half-sine pulse shaping. The signal in solid black line, $\hat{s}_C$, represents symbol C, while the waveform in the dashed blue line, $\hat{s}_3$, encodes symbol 3 (the least significant bits are encoded and transmitted first). Each chip has a duration of $2T_c$. The Q-phase chips are delayed by T_c with respect to I-phase chips.

the 2450 MHz DSSS PHY [9, p. 469] are reported in Table 1, where each PN sequence starts with a binary value of chip 0 and ends with a value of chip 31. The in-phase carrier transports even-indexed chips, while the quadrature-phase carries odd-indexed chips [9, p. 470]. Subsequent NRZ encoding transforms the zeros into negative ones.

Section VIII-A provides a detailed analysis of the codes in Table 1. The following section, instead, presents the phenomena that alter the transmitted signal.

B. CHANNEL IMPAIRMENTS

This section analytically describes a radio-propagation environment that alters the transmitted signals. We assume that path loss, shadow fading, and residual power fluctuations left by power control affect the transmitted SoI, whereas the interfering signals undergo free-space path loss increased by an attenuation factor that accounts for propagation obstacles. It is worth noting that although power control is not provided in all considered standards, we model this functionality for the sake of generality. The effect of multipath fading [64] should be compensated by the power control when available or neglected. This last assumption is also justified by the fact that highly absorbing environments in an industrial setting may eliminate multipath propagation [65]. Furthermore, a log-normal random variable with appropriate mean and variance values can closely approximate a composite Nakagami log-normal random variable, accounting for the combined effect of multipath fading and log-normal shadowing [66, pp. 113–114]. We represent the free-space path loss, ς_f, in the 2450 MHz band as in the IEEE 802.15.4 standard [9, p. 49] two-slope model [67, p. 19]:

$$\varsigma_f(d_i) = \begin{cases} 40.2 + 20\log_{10}(d_i) & \text{if } d_i \le 8, \\ 58.3 + 33\log_{10}(\frac{d_i}{8}) & \text{otherwise,} \end{cases} \tag{5}$$

where d_i indicates the distance between the ith transmitter and the reference receiver (Rx). The index $i = s$ indicates the transmitter sending the SoI, and $i \geq 0$ indicates an interfering transmitter. For alternative parameterizations of the path-loss model, see, for example, [68], [69], [70], and [71]. The path loss coefficient used in our model is

$$\alpha_i = 10^{-\frac{\varsigma_f(d_i)}{10}}. \tag{6}$$

We describe the shadow fading process that influences the transmitted signals via the log-normal model [64], which was investigated for indoor propagation environments in [72] and [73]. According to this model, the shadow fading contribution in dB, indicated by the term $\beta_i(t)$, has a normal distribution with mean $\mu_{\beta i}$, variance $\sigma^2_{\beta i}$, and a squared exponential correlation function:

$$\rho_{\beta i}(\tau) = \sigma^2_{\beta i}\, e^{-\frac{1}{2}\left(\frac{v_i \tau}{\Delta_i}\right)^2}. \tag{7}$$

In (7), Δ_i denotes the typical decorrelation decay distance, and v_i indicates either the field device speed if the field device is mobile [74] or the speed of the moving reflectors in the propagation environment. Notably, the mean value $\mu_{\beta i}$ is an additional attenuation factor that accounts for indoor obstacles, such as walls and floors, separating different environments. To streamline the presentation by avoiding the tedious technical description of moment-matching approximation [66, pp. 147–155], [75], we set $\sigma^2_{\beta i} = 0$ for $i \geq 0$ so that $\mu_{\beta i}$ fully characterizes the interference power attenuation owing to the obstacles. Finally, we model the residual power control error (PCE) in log units, indicated by $\xi_s(t)$, affecting the SoI by a zero-mean normal distribution with variance σ_e^2 and autocovariance

$$\rho_\xi(\tau) = \sigma_\xi^2\, e^{-\frac{1}{2}\left(\frac{\tau}{\tau_\xi}\right)^2}, \tag{8}$$

where τ_ξ is the decorrelation time within which the PCE is significant [76], and $\sigma_\xi = \frac{\ln 10}{10}\sigma_e$.

C. RECEIVER MODEL

The channel impairments presented above, AWGN, and wideband interference affect the SoI at the receiver input. The interference itself suffers from propagation impairments. Consequently, we write the signal at the receiver input (i.e., at the output of the communication channel) as

$$\mathcal{Y}(t) = c(t)\mathcal{X}(t) + \mathcal{W}(t) + \sum_{\iota=0}^{n_\Upsilon+1} (\mathcal{V}_{u\iota}(t) + \mathcal{V}_{d\iota}(t)). \tag{9}$$

In (9), $\mathcal{V}_{u\iota}(t)$ and $\mathcal{V}_{d\iota}(t)$ represent the interference caused by the ιth uplink and downlink transmissions from the IEEE 802.11n network colliding with the SoI, $\mathcal{W}(t)$ is the AWGN with a single-sided PSD N_0, and $c(t)$ is a positive real-valued factor that accounts for the channel impairments presented in Section VI-B and the SoI amplification $\sqrt{E_c}$ by the sender, where $\sqrt{E_c}$ is the chip energy [62, p. 403]. We model $c(t)$ as a correlated random process whose realizations are constant for the duration of a signal that transports one IEEE 802.15.4 PPDU.

$$c(t) = \sqrt{E_c}\;\alpha_s e^{\frac{\chi_s(t)}{2}} = \hat{c}_t, \tag{10}$$

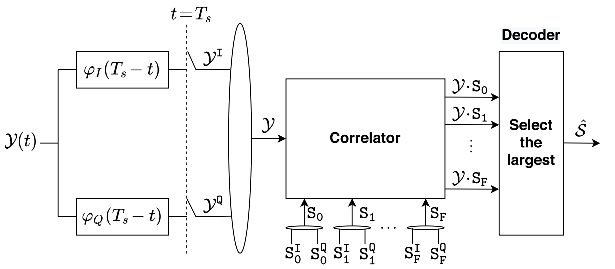

FIGURE 6. The matched filter implementation of the receiver. The input signal $\mathcal{Y}(t)$ is multiplied with the basis functions $\varphi_j(T_s - t)$ and sampled at T_s, producing a vector $\mathcal{Y}$ for every received symbol. The correlator block matches this vector to signals corresponding to each symbol of the alphabet, providing as output the correlation metrics. The decoder block selects the symbol with the largest metric.

where $\chi_s(t) = \xi_s(t) + \beta_s(t)$ is the contribution of correlated shadow fading and PCE, which are constant during the transmission interval, and $\hat{c}_t$ is the value of $c(t)$ at time t. If we denote by T_s the inverse of the symbol rate (which is 62.5 ksymbol/s), then the duration of the SoI is $n_s T_s$. Since for the IEEE 802.15.4 2450 MHz DSSS PHY the maximal size of the PPDU is 133 octets [9, pp. 460, 467, 468], this duration lasts at most 4.256 ms. Finally, we model the interference contributions of $\mathcal{V}_{u\iota}(t)$ and $\mathcal{V}_{d\iota}(t)$ to the received signal as a band-limited AWGN with variance $\sigma^2_{\mathcal{V}_i} = \alpha_i^2 e^{\mu_{\beta i}} \zeta \mathcal{P}_i$, where $i \leq n_A$ indicates an interfering device with a transmit power $\mathcal{P}_i$. We assume coherent demodulation and a good phase estimate of the carrier at the receiver, which thus can decompose the signal in (9) into its in-phase and quadrature components (see, e.g., [60] for a detailed discussion of the OQPSK-DSSS demodulation and [61] as an example of the architecture of a dual-mode IEEE 802.15.4 receiver that includes a QPSK demodulator chain). In such a scenario, the matched filter and correlation receivers achieve the minimum error probability for the AWGN channel and are equivalent in performance [62, Sec. 4.2-2, pp. 177–182]. Therefore, without loss of generality, we consider a matched-filter receiver sampled at T_s with 16 correlators that account for each data symbol within the alphabet. Fig. 6 shows the structure of this receiver performing optimal soft-decision decoding [62, Sec. 7.4, pp. 424–425, Sec. 4.2-1, pp. 170–171] under the assumption that all data symbols are equiprobable. Note that we made the equiprobable assumption only to streamline the presentation.

Let $\mathcal{Y}_\ell$ indicate the input of the correlator that corresponds to a received signal $\mathcal{Y}(t)$ segment transporting $\mathcal{X}_\ell$. Then, $\mathcal{Y}_\ell^\mathtt{I}$ and $\mathcal{Y}_\ell^\mathtt{Q}$ represent the I and Q components of the vector $\mathcal{Y}_\ell$. The outputs of the correlator in Fig. 6 are the inner products $\{\mathcal{Y}_\ell \cdot \mathtt{S}_\mathtt{i}\}_{\mathtt{i}=0}^{\mathtt{F}}$, commonly known as correlation metrics (CMs) for the soft-decision decoding. Formally, from (1)–(4), and (9), the definition of the inner product [62, Sec. 2.2-1, p. 28], and recognizing that we deal with real-valued signals, we have

$$\mathcal{Y}_\ell \cdot \mathtt{S}_\mathtt{i} = \mathcal{Y}_\ell^\mathtt{I} \mathtt{S}_\mathtt{i}^\mathtt{I} + \mathcal{Y}_\ell^\mathtt{Q} \mathtt{S}_\mathtt{i}^\mathtt{Q}, \tag{11}$$

$$\mathcal{Y}_\ell^\mathtt{I} \mathtt{S}_\mathtt{i}^\mathtt{I} = \int_{\ell T_s}^{(\ell+1)T_s} \mathcal{Y}(t)\, \varphi_I(t) \mathtt{S}_\mathtt{i}^\mathtt{I} dt, \tag{12}$$

$$\mathcal{Y}_\ell^\mathtt{Q} \mathtt{S}_\mathtt{i}^\mathtt{Q} = \int_{\ell T_s + T_c}^{(\ell+1)T_s + T_c} \mathcal{Y}(t)\, \varphi_Q(t) \mathtt{S}_\mathtt{i}^\mathtt{Q} dt. \tag{13}$$

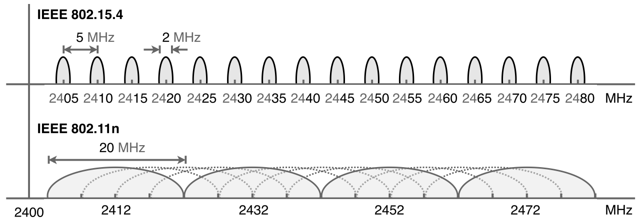

FIGURE 7. Overlapping map of the IEEE 802.15.4 and 802.11n radio channels.

The decoder output is a symbol providing the largest CM:

$$\hat{\mathtt{s}} = \arg \max_{0 \leq \mathtt{i} \leq \mathtt{F}} (\mathcal{Y}_\ell \cdot \mathtt{S}_\mathtt{i}). \tag{14}$$

If this symbol is different from that sent by the reference user, that is, if $\hat{\mathtt{s}} \neq \mathtt{s}$, we have a symbol error. By the linearity of the integration and (9), we decompose (12) and (13) into terms related to the SoI, interference, and AWGN:

$$\mathcal{Y}_\ell^\mathtt{I} \mathtt{S}_\mathtt{i}^\mathtt{I} = \mathrm{Y}_{\ell|\mathtt{i}}^\mathtt{I} + \mathrm{W}_{\ell|\mathtt{i}}^\mathtt{I} + \sum_{\iota=0}^{n_\Upsilon+1} \left(\mathrm{V}_{u\iota,\ell|\mathtt{i}}^\mathtt{I} + \mathrm{V}_{d\iota,\ell|\mathtt{i}}^\mathtt{I} \right), \tag{15}$$

$$\mathrm{Y}_{\ell|\mathtt{i}}^\mathtt{I} = \hat{c}_t \int_{\ell T_s}^{(\ell+1)T_s} \mathcal{X}_\ell\, \varphi_I(t)\, \mathtt{S}_\mathtt{i}^\mathtt{I} dt, \tag{16}$$

$$\mathrm{W}_{\ell|\mathtt{i}}^\mathtt{I} = \int_{\ell T_s}^{(\ell+1)T_s} \mathcal{W}(t)\, \varphi_I(t)\, \mathtt{S}_\mathtt{i}^\mathtt{I} dt, \tag{17}$$

$$\mathrm{V}_{j\iota,\ell|\mathtt{i}}^\mathtt{I} = \int_{\ell T_s}^{(\ell+1)T_s} \mathcal{V}_{j\iota}(t)\, \varphi_I(t)\, \mathtt{S}_\mathtt{i}^\mathtt{I} dt, \tag{18}$$

where $j \in \{u, d\}$, and the expressions of the quadrature-phase components follow a similar pattern. These terms are central to deriving the SINR and packet error probability discussed in Sections VIII-B and VIII-C. The computation of (16) and (17) involves splitting the integration interval into 16 parts corresponding to each reference user data chip, exploiting the linearity of the integration and some properties of the trigonometric functions. Furthermore, the term $\mathtt{S}_\mathtt{i}^\mathtt{I}$ in (16) and (17) requires a closer examination of the symbol-to-chip mapping presented in Table 1.

VII. IEEE 802.11 INTERFERENCE CHARACTERIZATION

In addition to being fundamental for implementing the first step of the framework described in Section V, this section also describes a new contribution in the context of analytical link modeling, independent of the co-design aspect. We focus on the IEEE 802.11n standard [55, Clause 19] operating in the 2.4 GHz industrial, scientific, and medical (ISM) radio band on 13 overlapping channels with a bandwidth of 20 MHz and center frequencies $f_C = 2407 + 5c$, where $c \in \{1, 2, \ldots, 13\}$ is the channel number. Fig. 7 illustrates the frequency overlap between IEEE 802.15.4 and 802.11n radio channels. Since the bandwidth of the IEEE 802.11 signals is much larger than that of the IEEE 802.15.4 signals (i.e., 2 MHz), following [13] and [67], we model the

TABLE 2. Interference power ratio values for different channels.

$n_C \backslash c$	1	2	3	4	5	6	7	...	13
11	**0.11198**	0.00021	0.00001	0.00000	0.00000	0.00000	0.00000	...	0.00000
12	**0.11236**	**0.11198**	0.00021	0.00001	0.00000	0.00000	0.00000	...	0.00000
13	**0.11244**	**0.11236**	**0.11198**	0.00021	0.00001	0.00000	0.00000	...	0.00000
14	**0.10655**	**0.11244**	**0.11236**	**0.11198**	0.00021	0.00001	0.00000	...	0.00000
15	0.00011	**0.10655**	**0.11244**	**0.11236**	**0.11198**	0.00021	0.00001	...	0.00000
16	0.00000	0.00011	**0.10655**	**0.11244**	**0.11236**	**0.11198**	0.00021	...	0.00000
17	0.00000	0.00000	0.00011	**0.10655**	**0.11244**	**0.11236**	**0.11198**	...	0.00000
18	0.00000	0.00000	0.00000	0.00011	**0.10655**	**0.11244**	**0.11236**	...	0.00000
19	0.00000	0.00000	0.00000	0.00000	0.00011	**0.10655**	**0.11244**	...	0.00000
20	0.00000	0.00000	0.00000	0.00000	0.00000	0.00011	**0.10655**	...	0.00000
21	0.00000	0.00000	0.00000	0.00000	0.00000	0.00000	0.00011	...	0.00001
22	0.00000	0.00000	0.00000	0.00000	0.00000	0.00000	0.00000	...	0.00021
23	0.00000	0.00000	0.00000	0.00000	0.00000	0.00000	0.00000	...	**0.11198**
24	0.00000	0.00000	0.00000	0.00000	0.00000	0.00000	0.00000	...	**0.11236**
25	0.00000	0.00000	0.00000	0.00000	0.00000	0.00000	0.00000	...	**0.11244**
26	0.00000	0.00000	0.00000	0.00000	0.00000	0.00000	0.00000	...	**0.10655**

interfering signals as band-limited AWGN. To estimate its PSD, we rely on analytical expressions for orthogonal frequency-division multiplexing (OFDM) signals from [77] parameterized according to the IEEE 802.11n standard requirements. Specifically, the IEEE 802.11n interfering-signal PSD for the 16-QAM subcarrier modulation is as follows:

$$S(f) = \frac{1}{T_S} \sum_{\substack{n=-n_S/2 \\ n\neq 0}}^{n_S/2} |\Psi(f - f_C - n\Delta_F)|^2 \,, \text{ where}$$
$$\Psi(f) = \frac{\sin(\pi f T_S)}{\pi f} \frac{\cos(\pi f T_T)}{1 - 4f^2 T_T^2}, \tag{19}$$

$T_S = 4\,\mu$s is the OFDM symbol interval, $n_S = 56$ is the total number of subcarriers, and $\Delta_F = 312.5$ kHz is the subcarrier frequency spacing [55, Table 19-6, p. 2879], while $T_T = 0.1\,\mu$s is the transition time of the windowing function applied to OFDM symbols [55, pp. 2811, 2935]. For alternative expressions for the PSD of OFDM signals, see, for instance, [78] and [79] and references therein.

The portion of the IEEE 802.11 signal power producing inband interference for the SoI depends on the frequency offset between the respective center frequencies. The following is a simple analytical expression of the interference power ratio due to the frequency offset:

$$\zeta = \frac{2\int_{-\infty}^{\infty} S(f) h\left(\frac{f-f_c}{B_c}\right) df}{\int_{-\infty}^{\infty} S(f) df}, \tag{20}$$

where B_c is the SoI bandwidth, and $f_c = 2405 + 5(n_c - 11)$ is the IEEE 802.15.4 2450 MHz DSSS PHY center frequency for the channel number $n_c \in \{11, 12, \ldots, 26\}$ [9, p. 430]. Table 2 presents the values of the interference power ratio for the considered radio channels. Notably, this table has the structure of a band matrix.

To analyze the worst impact of the IEEE 802.11 network on the LoI, we assumed that the interfering network operates in a saturated condition, modeled as in [15]. Denoting by ψ the probability that an 802.11 station transmits during a generic slot time and by υ the probability that a transmitted frame collides, the following equations characterize the saturated network operation.

$$\psi = \frac{1}{1 + \frac{1-\upsilon}{2(1-\upsilon^{R+1})}\left(\sum_{n=0}^{R} \upsilon^n (2^n W - 1) - \left(1 - \upsilon^{R+1}\right)\right)}, \tag{21}$$
$$\upsilon = 1 - (1 - \psi)^{n_T - 1}, \tag{22}$$

where R is the predefined retransmission/retry limit, W is the initial backoff window size, and n_T is the total number of stations in the IEEE 802.11 network. The numerical solution of (21) and (22) in ψ and υ provides the value of ψ used in the following expressions of the probabilities related to the events characterizing the timing between consecutive IEEE 802.11 frame transmissions by different nodes within a network. The probability that the IEEE 802.11n radio channel is busy because of transmission from any node in the network is

$$\varrho = 1 - (1 - \psi)^{n_T}. \tag{23}$$

As shown in Fig. 1, we consider $n_A \le n_T$ IEEE 802.11n devices, whose activity affects the LoI. The remaining $n_T - n_A$ nodes in the IEEE 802.11n network do not disturb the LoI because of the long distance or heavy attenuation due to obstacles on the propagation path to the reference user. Thus, we express the probability of successful transmission by one of $m \le n_T$ IEEE 802.11n devices as

$$\varpi(m) = m\psi(1 - \psi)^{n_T - 1}, \tag{24}$$

The probability of a collision owing to simultaneous transmission by κ among m interfering nodes is as follows:

$$\eta(m, \kappa) = \binom{m}{\kappa} (1 - \psi)^{m-\kappa} \psi^{\kappa}. \tag{25}$$

Finally, the total collision probability owing to concurrent transmissions within a set of m IEEE 802.11n devices is

$$\hat{\eta}(m) = \sum_{\kappa=2}^{m} \eta(m, \kappa) = 1 - (1-\psi)^m - m\psi\,(1-\psi)^{m-1}, \tag{26}$$

where the second equality follows from the binomial expansion of $((1 - \psi) + \psi)^m$.

The average period in which the IEEE 802.11n channel is free from transmissions that affect the LoI after a successful or colliding transmission from any interfering node is as follows:

$$\Phi(n_A) = \frac{(1-\varrho)T_E + \varpi\left(n_T - n_A\right)T_O + \left(\hat{\eta}(n_T) - \hat{\eta}(n_A)\right)T_M}{\varpi(n_A) + \hat{\eta}(n_A)}, \tag{27}$$

where T_E is the empty IEEE 802.11n slot time, T_O indicates the average time a successful transmission occupies the radio channel, and T_M denotes the average time the channel experiences a collision due to multiple simultaneous transmissions. Thus, the average time lapse between two consecutive IEEE 802.11n frame transmissions by interfering devices is

$$\Upsilon(n_A) = \frac{\varpi(n_A)\left(T_O + \Phi(n_A)\right) + \hat{\eta}(n_A)\left(T_M + \Phi(n_A)\right)}{\varpi(n_A) + \hat{\eta}(n_A)}. \tag{28}$$

TABLE 3. IEEE 802.11n network parameters used in the analysis.

Parameter	Value
W	15
T_A	28 μs
T_D	$T_I + 2T_E$
T_E	9 or 20 μs
T_F	28 μs
T_I	10 μs
T_P	0.4, 2, or 10 ms
T_R	30 μs

The average time components characterizing (27) and (28) are expressed as follows [15]:

$$T_O = \frac{WT_B}{W-1} + T_E, \tag{29}$$

$$T_M = T_C + T_E, \tag{30}$$

where T_B is the time interval in which the IEEE 802.11n channel is sensed as busy owing to a successful single-frame transmission and T_C indicates the channel collision time.

For the primary basic medium access mechanism, we have

$$T_B = T_C = T_P + T_I + T_A + T_D, \tag{31}$$

where T_P, T_I, T_A, and T_D are the time taken to transmit a PPDU, short interframe space (SIFS) time, time taken to transmit an acknowledgment (ACK), and distributed interframe space (DIFS) time, respectively.

When IEEE 802.11n packet transmission relies on the optional request-to-send/clear-to-send (RTS/CTS) mechanism instead of the basic mechanism, the expressions for T_B and T_C change as follows [15]:

$$T_B = T_R + T_F + 3T_I + T_P + T_A + T_D, \tag{32}$$

$$T_C = T_R + T_I + T_A + T_D, \tag{33}$$

where T_R is the time required to transmit an RTS frame and T_F is the CTS frame transmission time. Table 3 reports the values of these time parameters according to the IEEE 802.11n specification [55, pp. 796–797, 1681–1682, 2858, 2929, and 2951] for 16-QAM subcarrier modulation, response rate of 24 Mb/s, and mandatory 39 Mb/s data rate [55, p. 2952]. The PPDU sizes that determined the T_P values in Table 3 were 1950, 9750, and 48750 B.

The number n_c of collisions between IEEE 802.11n- and 802.15.4-compliant signals depends on their relative timings. An IEEE 802.15.4 signal transporting a control system payload lasts between 0.512 ms (i.e., the case of only one sensing or actuation variable in double-precision floating-point format delivered in the LLDN mode) and 3.776 ms (for eight variables in double format over WirelessHART protocol). Thus, when IEEE 802.11 stations send shorter signals (e.g., 0.4 ms long), symbols within any control system-related IEEE 802.15.4 PPDU may undergo different collisions owing to the temporal overlap with signals from various interfering IEEE 802.11 stations. See, for example, [13] for an analysis of such a case. By contrast, all symbols of most IEEE 802.15.4 PPDUs experience only a collision from

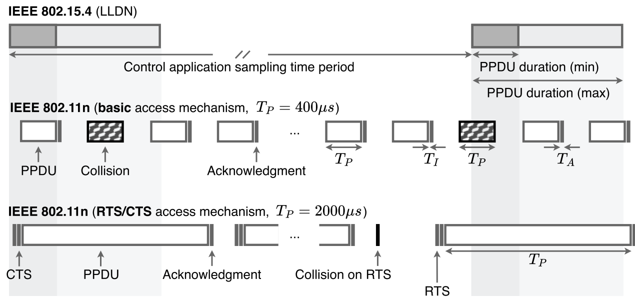

FIGURE 8. Collision time between IEEE 802.15.4 and IEEE 802.11n transmissions. Eight over ten IEEE 802.11n stations create interference on the LoI and have a 20% probability of collision between their frames.

one IEEE 802.11 station if the interfering network transmits predominantly longer than LoI signals. Such a situation occurs with 10 ms lasting IEEE 802.11n-compliant signals. Fig. 8 depicts these different cases. The collisions between interfering IEEE 802.11n signals result in more substantial interference power. If the IEEE 802.11n network uses the RTS/CTS medium-access mechanism, these collisions occur only on the RTS frames.

We distinguish between SoI collisions with IEEE 802.11n transmissions in the uplink (RTS and PPDU) and downlink (CTS and ACK). Notably, if an access point is among the interfering devices, we must consider the impact of its ACK and CTS frames on the LoI, in addition to the uplink transmissions from the IEEE 802.11n stations. Otherwise, when IEEE 802.11n access point transmissions do not affect the LoI, we still need to account for the ACK and CTS frames sent from interfering stations to their access points in response to the received communications. Thus, we have four different scenarios depending on the IEEE 802.11n network medium access mechanism (basic one or RTS/CTS) and the presence of access points among the interfering devices. For each scenario, let T_U denote the IEEE 802.15.4 PPDU duration, $T_U \in [512, 3776]\,\mu$s. The expected number of collisions with interfering signals depends on the time offset O between IEEE 802.15.4 and 802.11n transmissions. This time offset is not constant because of the different message-generation frequencies. As in [13], we assume that O has a uniform distribution in $\big[0, \Upsilon(n_A)\big)$. Consider

$$n_\Upsilon \triangleq \left\lfloor \frac{T_U}{\Upsilon(n_A)} \right\rfloor, \tag{34}$$

$$\varepsilon(n_A) \triangleq T_U - n_\Upsilon \Upsilon(n_A). \tag{35}$$

For $\iota \in \{0, 1, \ldots, n_\Upsilon + 1\}$, let $\Xi_R(O, \iota)$, $\Xi_C(O, \iota)$, $\Xi_P(O, \iota)$, and $\Xi_A(O, \iota)$ denote the collision duration between the ιth RTS, CTS, PPDU, and ACK frame from the IEEE 802.11n network and SoI. In particular, we consider as first the IEEE 802.11n frame that starts after the beginning of the IEEE 802.15.4 transmission on the LoI with a delay of at most O. Thus, $\iota = 0$ indicates the last IEEE 802.11n transmission started before that of the SoI.

We consider the first scenario with the basic medium access mechanism when IEEE 802.11n access points interfere with the LoI. If $n_\Upsilon \geq 1$, that is, if $T_U \geq \Upsilon(n_A)$, then $n_\Upsilon - 1$ IEEE 802.11n PPDUs and the related ACKs of successful transmissions will always collide with the SoI. Furthermore, depending on the values of the time offset O and parameter $\varepsilon(n_A)$, up to three additional IEEE 802.11n PPDUs and ACKs interfere with the IEEE 802.15.4 PPDU transmission. Specifically, (36)–(43), as shown at the bottom of the next page, characterize the collision times for $n_\Upsilon \geq 1$. If $T_U < \Upsilon(n_A)$, then $n_\Upsilon = 0$, and only two IEEE 802.11n PPDUs and their ACKs can interfere with the IEEE 802.15.4 PPDU. Furthermore, from (35), $\varepsilon(n_A) = T_U$ for $n_\Upsilon = 0$, and (36), (37), (42), and (43) describe the relevant collision times.

Our second reference scenario considers the basic medium access mechanism without IEEE 802.11n access points among the interfering devices. The access point ACKs do not affect the SoI, but the ACKs from the interfering IEEE 802.11n stations to their access points still create disturbances in the LoI. Denoting by n_P the number of access points connecting the n_S interfering stations to the IEEE 802.11n network, the adequate number of interfering devices to consider is $n_A = n_P + n_S$. The collision duration still obeys expressions (36)–(43), but for each $\iota \in \{0, 1, \ldots, n_\Upsilon + 1\}$ the collision occurs exclusively on a PPDU or ACK and not on both.

The remaining scenarios consider the RTS/CTS medium access mechanism and thus account for two additional short transmissions (RTS and CTS). However, the collision duration expressions follow a logic similar to that in (36)–(43). Therefore, we did not report their explicit expressions.

VIII. MESSAGE ERROR PROBABILITY DERIVATION

In Section IV, we showed that end-to-end message dropout in multi-hop WNCSs comprises the ever-present PHY packet losses and possible MAC-induced frame losses in wireless single-hop links, potential network packet losses caused by excessive traffic load on network nodes, and message discarding by message disorder-handling mechanisms at the application layer on endpoints. These four factors that contribute to overall message dropout are nearly independent. PHY packet losses arise from detected channel decoder errors induced by the physical characteristics of the propagation environment, including several interference types, as described in Sections IV-B1 and VI-B. Determining the detection scheme error probability requires considering the values of all parameters and variables in Fig. 3 that are relevant for a considered scenario. This section shows how to do so via an analytical procedure expressing the PPDU dropout as the probability that a random variable exceeds a specific value. The resulting likelihood is a function of the SINR and is thus suitable for constructing FSMC models, leading to Markov jump system abstractions that are widely used for WNCS analysis and design [7]. MAC-induced frame losses occur when timely access to a communication channel via contention-based protocol fails. Representing a MAC algorithm through a Markov chain [20] leads to analytical expressions of frame-discard probabilities for each communication link. These probabilities are independent of the PPDU dropout probabilities on the same link and frame discard probabilities on different links. Estimating the network packet loss probability due to node buffer overflow relies on queuing theory, specifically finite queue analysis [20], [80]. Network congestion control algorithms use this metric under the names of buffer drop rate, queue loss ratio, rejection rate, or blocking probability in their approaches to mitigate the effect of detected congestion [81]. Notably, the node-related network packet loss process is independent of the link-related PPDU dropouts and MAC-induced frame losses. Finally, outdated message discarding, also known as message rejection [82], occurs when more recent data become available before older data use or when end-to-end message delay exceeds a specific threshold, such as a plant sampling period [7]. Thus, deriving the probability of such an event relies heavily on applicable stochastic delay models that may account for the retransmission, MAC, and queuing delays. The resulting correlation with the PHY packet loss probability found in scenarios in which time diversity is deployed complicates the analysis.

The following sections present the explicit derivation of the PPDU dropout probability considering the chip sequence structure contributions and its use in message loss probability deduction and the WNCS controller design.

A. INFORMATION-THEORETIC ASPECTS OF DEMODULATION

When $\mathcal{X}_\ell$ from (4) modulates a data symbol $\ddot{\mathtt{i}}$ different from $\mathtt{i}$, we find in (16) the term $\mathcal{S}^I_\ell \mathtt{S}^{\mathtt{I}}_{\mathtt{i}} \neq (\mathtt{S}^{\mathtt{I}}_{\mathtt{i}})^2$, which means that the result of data chip multiplication does not always equal to 1: if the values of data chips having the same index are different, their product value is -1. The Hamming distance between $\mathcal{S}^I_\ell = \mathtt{S}^{\mathtt{I}}_{\ddot{\mathtt{i}}}$ and $\mathtt{S}^{\mathtt{I}}_{\mathtt{i}}$, denoted by $\Delta(\mathtt{S}^{\mathtt{I}}_{\ddot{\mathtt{i}}}, \mathtt{S}^{\mathtt{I}}_{\mathtt{i}})$, provides the number of positions at which the corresponding sequences of the data chips differ. Among 16 data chips of $\mathcal{S}^I_\ell$ there are $16 - \Delta(\mathtt{S}^{\mathtt{I}}_{\ddot{\mathtt{i}}}, \mathtt{S}^{\mathtt{I}}_{\mathtt{i}})$ chips matching the values of chips in $\mathtt{S}^{\mathtt{I}}_{\mathtt{i}}$, and $\Delta(\mathtt{S}^{\mathtt{I}}_{\ddot{\mathtt{i}}}, \mathtt{S}^{\mathtt{I}}_{\mathtt{i}})$ chips with the same index but opposite values. Thus, the sum of the corresponding data chip products is

$$\varkappa^{\mathtt{II}}_{\ddot{\mathtt{i}}\mathtt{i}} \triangleq 16 - 2\Delta(\mathtt{S}^{\mathtt{I}}_{\ddot{\mathtt{i}}}, \mathtt{S}^{\mathtt{I}}_{\mathtt{i}}),$$

and, $\forall \mathtt{i}, \ddot{\mathtt{i}} \in \{\mathtt{0}, \mathtt{1}, \ldots, \mathtt{F}\}$, the expression of (16) becomes

$$\mathrm{Y}^{\mathtt{I}}_{\ell|\mathtt{i}} = \varkappa^{\mathtt{II}}_{\ddot{\mathtt{i}}\mathtt{i}} \hat{c}_t \quad \text{for} \quad \mathcal{X}_\ell = \mathtt{S}^{\mathtt{I}}_{\ddot{\mathtt{i}}} \varphi_I(t) - \mathtt{S}^{\mathtt{Q}}_{\ddot{\mathtt{i}}} \varphi_Q(t). \tag{44}$$

The same reasoning applies to the Q-phase components and, more generally, to all NRZ encoded sequences of the same length. Thus, for $\mathtt{j}, \ddot{\mathtt{j}} \in \{\mathtt{I}, \mathtt{Q}\}$ and $\mathtt{i}, \ddot{\mathtt{i}} \in \{\mathtt{0}, \mathtt{1}, \ldots, \mathtt{F}\}$, we define

$$\varkappa^{\ddot{\mathtt{j}}\mathtt{j}}_{\ddot{\mathtt{i}}\mathtt{i}} \triangleq 16 - 2\Delta(\mathtt{S}^{\ddot{\mathtt{j}}}_{\ddot{\mathtt{i}}}, \mathtt{S}^{\mathtt{j}}_{\mathtt{i}}). \tag{45}$$

Since the Hamming distance between a sequence and itself is 0, we have that $\varkappa^{\mathtt{jj}}_{\mathtt{ii}} = 16$ for all $\mathtt{i}$ and $\mathtt{j}$. Computing $\varkappa^{\ddot{\mathtt{j}}\mathtt{j}}_{\ddot{\mathtt{i}}\mathtt{i}}$ for all the symbols $\ddot{\mathtt{i}}$ and $\mathtt{i}$ in Table 1 reveals that the most uncommon are $\varkappa^{\mathtt{QQ}}_{\mathtt{19}} = \varkappa^{\mathtt{QQ}}_{\mathtt{91}} = -14$ and $\varkappa^{\mathtt{QQ}}_{\mathtt{1F}} = \varkappa^{\mathtt{QQ}}_{\mathtt{F1}} = 6$, while the typical values of $\varkappa^{\ddot{\mathtt{j}}\mathtt{j}}_{\ddot{\mathtt{i}}\mathtt{i}}$ are $\{-16, -8, -6, -4, -2, 0, 2, 4, 16\}$. The factors $\varkappa^{\ddot{\mathtt{j}}\mathtt{j}}_{\ddot{\mathtt{i}}\mathtt{i}}$ determine the receiver nominal performance by defining the

$$\Xi_P(O,0)=\begin{cases} 0 & \text{for } O\in[0,\,\Upsilon(n_A)-T_P);\\ O-(\Upsilon(n_A)-T_P) & \text{for } T_U > T_P \text{ and } O\in[\Upsilon(n_A)-T_P,\,\Upsilon(n_A));\\ O-(\Upsilon(n_A)-T_P) & \text{for } T_U \le T_P \text{ and } O\in[\Upsilon(n_A)-T_P,\,\Upsilon(n_A)-T_P+T_U);\\ T_U & \text{for } T_U < T_P \text{ and } O\in[\Upsilon(n_A)-T_P+T_U,\,\Upsilon(n_A)). \end{cases} \tag{36}$$

$$\Xi_A(O,0)=\begin{cases} 0 & \text{for } O\in[0,\,\Upsilon(n_A)-T_P-T_I-T_A);\\ O-(\Upsilon(n_A)-T_P-T_I-T_A) & \text{for } T_U \le T_A \text{ and } O\in[\Upsilon(n_A)-T_P-T_I-T_A,\,\Upsilon(n_A)-T_P-T_I-T_A+T_U);\\ T_U & \text{for } T_U \le T_A \text{ and } O\in[\Upsilon(n_A)-T_P-T_I-T_A+T_U,\,\Upsilon(n_A)-T_P-T_I);\\ \Upsilon(n_A)-T_P-T_I+T_U-O & \text{for } T_U \le T_A \text{ and } O\in[\Upsilon(n_A)-T_P-T_I,\,\Upsilon(n_A)-T_P-T_I+T_U);\\ 0 & \text{for } T_U \le T_A \text{ and } O\in[\Upsilon(n_A)-T_P-T_I+T_U,\,\Upsilon(n_A));\\ O-(\Upsilon(n_A)-T_P-T_I-T_A) & \text{for } T_U > T_A \text{ and } O\in[\Upsilon(n_A)-T_P-T_I-T_A,\,\Upsilon(n_A)-T_P-T_I);\\ T_A & \text{for } T_A<T_U\le T_P+T_I+T_A \text{ and } O\in[\Upsilon(n_A)-T_P-T_I,\\ & \qquad \Upsilon(n_A)-T_P-T_I-T_A+T_U);\\ T_A & \text{for } T_U > T_P+T_I+T_A \text{ and } O\in[\Upsilon(n_A)-T_P-T_I,\,\Upsilon(n_A));\\ \Upsilon(n_A)-T_P-T_I+T_U-O & \text{for } T_A<T_U\le T_P+T_I \text{ and } O\in[\Upsilon(n_A)-T_P-T_I-T_A\\ & \qquad +T_U,\,\Upsilon(n_A)-T_P-T_I+T_U);\\ \Upsilon(n_A)-T_P-T_I+T_U-O & \text{for } T_P+T_I<T_U\le T_P+T_I+T_A\\ & \qquad \text{and } O\in[\Upsilon(n_A)-T_P-T_I-T_A+T_U,\,\Upsilon(n_A));\\ 0 & \text{for } T_A<T_U<T_P+T_I \text{ and } O\in[\Upsilon(n_A)-T_P-T_I-T_A+T_U,\,\Upsilon(n_A)). \end{cases} \tag{37}$$

$$\Xi_P(O,\iota) = T_P \text{ for all } 0 < \iota < n_\Upsilon - 1. \tag{38}$$

$$\Xi_A(O,\iota) = T_A \text{ for all } 0 < \iota < n_\Upsilon - 1. \tag{39}$$

$$\Xi_P(O,n_\Upsilon)=\begin{cases} T_P & \text{for } \varepsilon(n_A) > T_P;\\ T_P & \text{for } \varepsilon(n_A) \le T_P \text{ and } O\in[0,\,\varepsilon(n_A)+\Upsilon(n_A)-T_P);\\ \varepsilon(n_A)+\Upsilon(n_A)-O & \text{for } \varepsilon(n_A) \le T_P \text{ and } O\in[\varepsilon(n_A)+\Upsilon(n_A)-T_P,\,\Upsilon(n_A)). \end{cases} \tag{40}$$

$$\Xi_A(O,n_\Upsilon)=\begin{cases} T_A & \text{for } \varepsilon(n_A)>T_P+T_I+T_A;\\ T_A & \text{for } \varepsilon(n_A)\le T_P+T_I+T_A \text{ and } O\in[0,\,\varepsilon(n_A)+\Upsilon(n_A)-T_P-T_I-T_A);\\ \varepsilon(n_A)+\Upsilon(n_A)-T_P-T_I-O & \text{for } T_P+T_I\le\varepsilon(n_A)\le T_P+T_I+T_A\\ & \qquad \text{and } O\in[\varepsilon(n_A)+\Upsilon(n_A)-T_P-T_I-T_A,\,\Upsilon(n_A));\\ \varepsilon(n_A)+\Upsilon(n_A)-T_P-T_I-O & \text{for } \varepsilon(n_A)<T_P+T_I\\ & \qquad \text{and } O\in[\varepsilon(n_A)+\Upsilon(n_A)-T_P-T_I-T_A,\,\varepsilon(n_A)+\Upsilon(n_A)-T_P-T_I);\\ 0 & \text{for } \varepsilon(n_A)<T_P+T_I \text{ and } O\in[\varepsilon(n_A)+\Upsilon(n_A)-T_P-T_I,\,\Upsilon(n_A)). \end{cases} \tag{41}$$

$$\Xi_P(O,n_\Upsilon+1)=\begin{cases} T_P & \text{for } \varepsilon(n_A) > T_P \text{ and } O\in[0,\,\varepsilon(n_A)-T_P);\\ \varepsilon(n_A)-O & \text{for } \varepsilon(n_A) > T_P \text{ and } O\in[\varepsilon(n_A)-T_P,\,\varepsilon(n_A));\\ 0 & \text{for } \varepsilon(n_A) > T_P \text{ and } O\in[\varepsilon(n_A),\,\Upsilon(n_A));\\ \varepsilon(n_A)-O & \text{for } \varepsilon(n_A) \le T_P \text{ and } O\in[0,\,\varepsilon(n_A));\\ 0 & \text{for } \varepsilon(n_A) \le T_P \text{ and } O\in[\varepsilon(n_A),\,\Upsilon(n_A)). \end{cases} \tag{42}$$

$$\Xi_A(O,n_\Upsilon+1)=\begin{cases} T_A & \text{for } \varepsilon(n_A)>T_P+T_I+T_A \text{ and } O\in[0,\,\varepsilon(n_A)-T_P-T_I-T_A);\\ \varepsilon(n_A)-T_P-T_I-O & \text{for } \varepsilon(n_A)>T_P+T_I+T_A \text{ and } O\in[\varepsilon(n_A)-T_P-T_I-T_A,\,\varepsilon(n_A)-T_P-T_I);\\ 0 & \text{for } \varepsilon(n_A)>T_P+T_I+T_A \text{ and } O\in[\varepsilon(n_A)-T_P-T_I,\,\Upsilon(n_A));\\ \varepsilon(n_A)-T_P-T_I-O & \text{for } T_P+T_I\le\varepsilon(n_A)\le T_P+T_I+T_A \text{ and } O\in[0,\,\varepsilon(n_A)-T_P-T_I);\\ 0 & \text{for } T_P+T_I\le\varepsilon(n_A)\le T_P+T_I+T_A \text{ and } O\in[\varepsilon(n_A)-T_P-T_I,\,\Upsilon(n_A));\\ 0 & \text{for } \varepsilon(n_A)<T_P+T_I. \end{cases} \tag{43}$$

TABLE 4. Factors defining the contribution of the SoI to CMs.

ï\i	0	1	2	3	4	5	6	7	8	9	A	B	C	D	E	F
0	**32**	2	−4	−8	−8	−8	−4	0	0	**8**	4	−8	−8	−8	4	**8**
1	2	**32**	2	−2	−10	−10	−6	−6	**6**	2	**6**	2	−6	−6	−10	**6**
2	−4	2	**32**	0	−4	−8	−8	−8	4	**8**	0	**8**	4	−8	−8	−8
3	−8	−2	0	**32**	0	−4	−8	−8	−8	4	**8**	0	**8**	4	−8	−8
4	−8	−10	−4	0	**32**	0	−4	−8	−8	−8	4	**8**	0	**8**	4	−8
5	−8	−10	−8	−4	0	**32**	0	−4	−8	−8	−8	4	**8**	0	**8**	4
6	−4	−6	−8	−8	−4	0	**32**	0	4	−8	−8	−8	4	**8**	0	**8**
7	0	−6	−8	−8	−8	−4	0	**32**	**8**	4	−8	−8	−8	4	**8**	0
8	0	6	4	−8	−8	−8	4	**8**	**32**	0	−4	−8	−8	−8	−4	0
9	**8**	2	**8**	4	−8	−8	−8	4	0	**32**	0	−4	−8	−8	−8	−4
A	4	6	0	**8**	4	−8	−8	−8	−4	0	**32**	0	−4	−8	−8	−8
B	−8	2	**8**	0	**8**	4	−8	−8	−8	−4	0	**32**	0	−4	−8	−8
C	−8	−6	4	**8**	0	**8**	4	−8	−8	−8	−4	0	**32**	0	−4	−8
D	−8	−6	−8	4	**8**	0	**8**	4	−8	−8	−8	−4	0	**32**	0	−4
E	4	−10	−8	−8	4	**8**	0	**8**	−4	−8	−8	−8	−4	0	**32**	0
F	**8**	6	−8	−8	−8	4	**8**	0	0	−4	−8	−8	−8	−4	0	**32**

term $\mathrm{Y}^{\mathtt{I}}_{\ell|\mathtt{i}} + \mathrm{Y}^{\mathtt{Q}}_{\ell|\mathtt{i}}$ that appears through (15) in (11) and consequently in (14). Table 4 reports the values of $\varkappa^{\mathtt{I}\mathtt{I}}_{\ddot{\mathtt{i}}\mathtt{i}} + \varkappa^{\mathtt{Q}\mathtt{Q}}_{\ddot{\mathtt{i}}\mathtt{i}}$ for all symbols $\mathtt{i}$, $\ddot{\mathtt{i}}$ from Table 1, showing that for each transmitted symbol $\ddot{\mathtt{i}}$, certain symbols $\mathtt{i} \neq \ddot{\mathtt{i}}$ have potentially larger CMs than others. For instance, symbols $\mathtt{9}$ and $\mathtt{F}$ are the closest to zero: they have the highest potential to produce a symbol error owing to AWGN and interference.

B. EXPLICIT ANALYTICAL MODEL OF SINR

The SINR is commonly used to measure the quality of wireless links. Networks based on IEEE 802.15.4-compatible hardware perform link quality indicator (LQI) measurements [9, p. 457] to estimate the received packet signal-to-noise ratio (SNR). The latest version of the standard (which is not yet supported by the considered industrial communication protocols) also defines a received signal noise indicator (RSNI) for frame-level SINR assessments [9, pp. 154 – 155].

The symbol-level SINR at the input of the correlator denoted by $\gamma_{\ell|\mathtt{i}}$ for the symbol $\mathtt{S}_{\mathtt{i}}$ is (46), as shown at the bottom of the next page, where $\mathbb{E}[\cdot]$ is the expected value. Without an interfering signal, $\gamma_{\ell|\mathtt{i}}$ provides symbol-level SNR [83]. By linearity of expectation, AWGN independence from the transmitted signals, and statistical independence of consecutive model slots for the interfering transmissions [15], an equivalent expression of the SINR is (47), as shown at the bottom of the next page. Since $\mathcal{W}(t)$ is the AWGN with a single-sided PSD N_0, from (17), (2), (3), $\omega_p = \frac{\pi}{2T_c}$, trigonometric identities, $T_s = 32T_c$, and low-pass filtering, we have that, for $\mathtt{j} \in \{\mathtt{I}, \mathtt{Q}\}$ and $\mathcal{S}_\ell = \mathtt{S}_{\ddot{\mathtt{i}}}$,

$$\mathbb{E}\left[\left(\mathrm{W}^{\mathtt{j}}_{\ell|\mathtt{i}}\right)^2\right] = \varkappa^{\mathtt{j}\mathtt{j}}_{\ddot{\mathtt{i}}\mathtt{i}} N_0. \tag{48}$$

To derive the interference contribution to the SINR, we need to account for the time offset O between the transmissions from different networks, the interfering network medium access mechanism, and interfering device characteristics such as transmit power, distance from the affected receiver, and whether the interfering node is a station or an access point. Assuming that each interfering station communicates with one specific access point, we indicate by $\mathcal{A}(i)$ the access point communicating with the ith station. As discussed in Section VII, these access points may not be part of a set of interfering devices. Without loss of generality, we index the interfering stations with integers $1 \leq i \leq n_s$ and access points with integers $n_s + 1 \leq j \leq n_s + n_p$. We denote the set of interfering stations linked to jth access point by $\mathcal{L}(j)$. In the following, we consider explicitly only the basic medium access mechanism: the ιth interfering transmissions $\mathcal{V}_{u\iota}(t)$ and $\mathcal{V}_{d\iota}(t)$ last $\Xi_P(O, \iota)$ and $\Xi_A(O, \iota)$, respectively. Any of the n_A devices from the interfering network can initiate a successful transmission affecting the SoI with the same probability $\varpi(n_A)$ from (24). Thus, a successful transmission by a specific interfering node has a discrete uniform distribution with a probability mass function $\frac{1}{n_A}$. Collisions between multiple simultaneous interfering transmissions produce a combined effect resulting in more substantial interference. As summarized by (25), $\binom{n_A}{\kappa}$ combinations of $\kappa \geq 2$ interfering nodes initiate a concurrent transmission with probability $(1-\psi)^{n_A - \kappa}\,\psi^{\kappa}$. For any κ-element subset ordering [84, Sec. 2.3, pp. 43 – 52], we enumerate the combinations from zero to $\binom{n_A}{\kappa} - 1$, thus giving the combinations a unique rank. We then denote the κ-element (index) subset with rank r as $\mathcal{U}(r)$. Since $T_s = 16\,\mu\text{s} < \Upsilon(n_A)$ for any IEEE 802.11n PPDU transmission duration T_P, only two different IEEE 802.11n PPDUs and their ACKs may affect the SoI symbol $\mathcal{S}_\ell$. Uplink and downlink interfering transmissions from the same slot suffer from distinct channel impairments owing to different propagation environments, rendering them statistically independent. Finally, from (36), (37), (42), and (43), for $T_U = T_s$, the expected relevant collision durations are as follows:

$$\mathbb{E}[\Xi_P(O, 0)] = \frac{\int_0^{\Upsilon(n_A)} \Xi_P(O, 0)\,dO}{\Upsilon(n_A)} = \frac{T_s T_P - \frac{1}{2}T_s^2}{\Upsilon(n_A)}, \tag{49}$$

$$\mathbb{E}[\Xi_A(O, 0)] = \frac{T_s T_A}{\Upsilon(n_A)}, \tag{50}$$

$$\mathbb{E}\big[\Xi_P(O, n_\Upsilon + 1)\big] = \frac{T_s^2}{2\Upsilon(n_A)}, \tag{51}$$

and

$$\mathbb{E}\big[\Xi_A(O, n_\Upsilon + 1)\big] = 0. \tag{52}$$

For notational convenience, we indicate a term proportional to the interference contribution to the SINR as follows:

$$\mathcal{E}^{\mathtt{j}}_{\ell|\mathtt{i}} \triangleq \frac{1}{\varkappa^{\mathtt{j}\mathtt{j}}_{\ddot{\mathtt{i}}\mathtt{i}} T_s} \sum_{\iota=0}^{n_\Upsilon + 1} \mathbb{E}\left[\left(\mathrm{V}^{\mathtt{j}}_{u\iota,\ell|\mathtt{i}} + \mathrm{V}^{\mathtt{j}}_{d\iota,\ell|\mathtt{i}}\right)^2\right], \tag{53}$$

where $\mathtt{j} \in \{\mathtt{I}, \mathtt{Q}\}$ and $\mathcal{S}_\ell = \mathtt{S}_{\ddot{\mathtt{i}}}$. From the considerations above and the same line of reasoning that brought (48), by (50) – (52), the law of total expectation and linearity of integration, we obtain (54), as shown at the bottom of the next page, for the first scenario with access points within the set of active interferers. The second scenario, without access points actively affecting the SoI, is obtained with a slight modification of the indices in (54), leading to (55), as shown at the bottom of the next page.

Notice from (54) and (55) that $\mathcal{E}^{\mathtt{j}}_{\ell|\mathtt{i}}$ is independent of $\mathtt{j}$, ℓ, and $\mathtt{i}$. We emphasize this observation through the second equality in (54) and (55). Thus, the interference contribution to the SINR depends on $\mathtt{j}$, ℓ, and $\mathtt{i}$ only through the proportional term of $\mathcal{E}^{\mathtt{j}}_{\ell|\mathtt{i}}$ in (53). From (44), (47), (48), (53), (54), and (55),

$$\gamma_{\ell|\mathtt{i}} = \frac{\hat{c}_t^2}{N_0 + T_s\mathcal{E}} \triangleq \hat{\gamma}_t, \tag{56}$$

where the second equality accentuates the independence of symbol-level SINR at the input of the correlator from the position ℓ of the received symbol within the SoI. In (56), $\hat{\gamma}_t$ indicates the value of the SINR $\gamma(t)$ corresponding to the log-normal process $c(t)$ in (10) with the value $\hat{c}_t$.

Fig. 9, 10, and 11 show the interference PSD $T_s\mathcal{E}$ for an increasing number of interfering devices, all transmitting at ten dBm at channel one and distant ten meters from the IEEE 802.15.4-compliant receiver operating at channel 11. The amount of received interference depends on the Wi-Fi network size, medium access mechanism and parameters, and number of devices directly affecting the reference receiver.

The following sections expand on the relationship between the frame-level SINR and PHY packet error probabilities.

C. PACKET ERROR PROBABILITY DERIVATION

This subsection presents a probabilistic analysis of the PER based on frame-level SINR measurements. The receiver considered in Section VI-C implements optimal soft-decision decoding, which selects symbols with the largest correlation metric (14). Formally, the decoding decision is correct if for any $\ell \in \{0, 1, \ldots, n_s\}$ and $\mathtt{i} \in \{\mathtt{0}, \mathtt{1}, \ldots, \mathtt{F}\}$, the encoded symbol $\mathtt{s} = \mathtt{i}$, and the difference between its CM $\mathcal{Y}_\ell \cdot \mathtt{S}_\mathtt{i}$ and any other CM is positive, i.e., it holds that $\mathrm{Z}_{\ell|\mathtt{il}} > 0$ $\forall \mathtt{l} \in \{\mathtt{0}, \mathtt{1}, \ldots, \mathtt{F}\}$ such that $\mathtt{l} \neq \mathtt{i}$, where

$$\mathrm{Z}_{\ell|\mathtt{il}} \triangleq \mathcal{Y}_\ell \cdot \mathtt{S}_\mathtt{i} - \mathcal{Y}_\ell \cdot \mathtt{S}_\mathtt{l}. \tag{57}$$

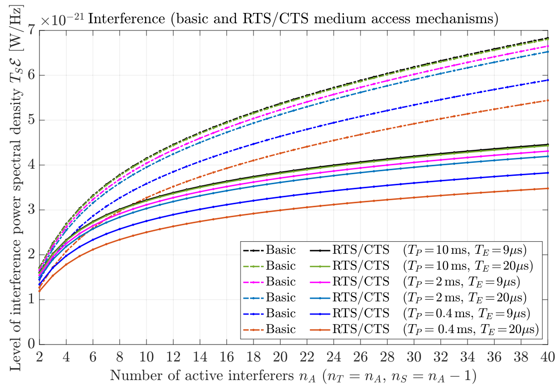

FIGURE 9. Interference PSD for the basic and RTS/CRS medium access mechanisms, one access point, and all devices within the Wi-Fi network interfering with the reference receiver. Such a scenario characterizes the upper bound on the received interference from a network with one access point. The Wi-Fi networks with the RTS/CRS medium access mechanism interfere less than those with basic medium access in all settings. Longer PPDUs with shorter empty slot times produce the most interference for any number of Wi-Fi devices in a network. Furthermore, the empty slot duration impact on interference significantly decreases for larger PPDUs.

By the law of total probability, for equiprobable symbols, the probability of a correct ℓth symbol detection event is

$$\mathrm{P}_{\mathrm{sd}|\ell} = \frac{1}{16}\sum_{\mathtt{i}=\mathtt{0}}^{\mathtt{F}} P\big(\mathrm{Z}_{\ell|\mathtt{il}} > 0,\ \mathtt{l} \neq \mathtt{i},\ \mathtt{l} \in \{\mathtt{0}, \ldots, \mathtt{F}\}\big). \tag{58}$$

Current IEEE 802.15.4-based communication standards do not implement forward error correction (FEC). Thus, even one erroneous symbol corrupts the entire message. As the symbol-detection error event is complementary to the correct symbol detection, the probability of PHY packet corruption

$$\gamma_{\ell|\mathtt{i}} \triangleq \frac{\left(\mathrm{Y}^{\mathtt{I}}_{\ell|\mathtt{i}}\right)^2 + \left(\mathrm{Y}^{\mathtt{Q}}_{\ell|\mathtt{i}}\right)^2}{\mathbb{E}\left[\left(\mathrm{W}^{\mathtt{I}}_{\ell|\mathtt{i}} + \sum_{\iota=0}^{n_\Upsilon+1}\left(\mathrm{V}^{\mathtt{I}}_{u\iota,\ell|\mathtt{i}} + \mathrm{V}^{\mathtt{I}}_{d\iota,\ell|\mathtt{i}}\right)\right)^2 + \left(\mathrm{W}^{\mathtt{Q}}_{\ell|\mathtt{i}} + \sum_{\iota=0}^{n_\Upsilon+1}\left(\mathrm{V}^{\mathtt{Q}}_{u\iota,\ell|\mathtt{i}} + \mathrm{V}^{\mathtt{Q}}_{d\iota,\ell|\mathtt{i}}\right)\right)^2\right]}. \tag{46}$$

$$\gamma_{\ell|\mathtt{i}} = \frac{\left(\mathrm{Y}^{\mathtt{I}}_{\ell|\mathtt{i}}\right)^2 + \left(\mathrm{Y}^{\mathtt{Q}}_{\ell|\mathtt{i}}\right)^2}{\mathbb{E}\left[\left(\mathrm{W}^{\mathtt{I}}_{\ell|\mathtt{i}}\right)^2\right] + \mathbb{E}\left[\left(\mathrm{W}^{\mathtt{Q}}_{\ell|\mathtt{i}}\right)^2\right] + \sum_{\iota=0}^{n_\Upsilon+1}\left(\mathbb{E}\left[\left(\mathrm{V}^{\mathtt{I}}_{u\iota,\ell|\mathtt{i}} + \mathrm{V}^{\mathtt{I}}_{d\iota,\ell|\mathtt{i}}\right)^2\right] + \mathbb{E}\left[\left(\mathrm{V}^{\mathtt{Q}}_{u\iota,\ell|\mathtt{i}} + \mathrm{V}^{\mathtt{Q}}_{d\iota,\ell|\mathtt{i}}\right)^2\right]\right)}. \tag{47}$$

$$\begin{aligned}\mathcal{E}^{\mathtt{j}}_{\ell|\mathtt{i}} = {} & \frac{\varpi(n_A)}{n_A}\left(\frac{T_P}{\Upsilon(n_A)}\sum_{i_1=1}^{n_A}\sigma^2_{\mathcal{V}i_1} + \frac{T_A}{\Upsilon(n_A)}\left(\sum_{i_2=1}^{n_S}\sigma^2_{\mathcal{V}\mathcal{A}(i_2)} + \sum_{i_3=n_S+1}^{n_A}\frac{1}{|\mathcal{L}(i_3)|}\sum_{i_4\in\mathcal{L}(i_3)}\sigma^2_{\mathcal{V}i_4}\right)\right) \\ & + \frac{T_P}{\Upsilon(n_A)}\sum_{\kappa=2}^{n_A}(1-\psi)^{n_A-\kappa}\,\psi^\kappa\sum_{i_5=0}^{\binom{n_A}{\kappa}-1}\ \sum_{i_6\in\mathcal{U}(i_5)}\sigma^2_{\mathcal{V}i_6} = \mathcal{E}.\end{aligned} \tag{54}$$

$$\mathcal{E}^{\mathtt{j}}_{\ell|\mathtt{i}} = \frac{\varpi(n_S)}{n_S}\left(\frac{T_P}{\Upsilon(n_A)}\sum_{i_1=1}^{n_S}\sigma^2_{\mathcal{V}i_1} + \frac{T_A}{\Upsilon(n_A)}\sum_{i_2=n_S+1}^{n_A}\frac{1}{|\mathcal{L}(i_2)|}\sum_{i_3\in\mathcal{L}(i_2)}\sigma^2_{\mathcal{V}i_3}\right) + \frac{T_P}{\Upsilon(n_A)}\sum_{\kappa=2}^{n_S}(1-\psi)^{n_S-\kappa}\,\psi^\kappa\sum_{i_4=0}^{\binom{n_S}{\kappa}-1}\ \sum_{i_5\in\mathcal{U}(i_4)}\sigma^2_{\mathcal{V}i_5} = \mathcal{E}. \tag{55}$$

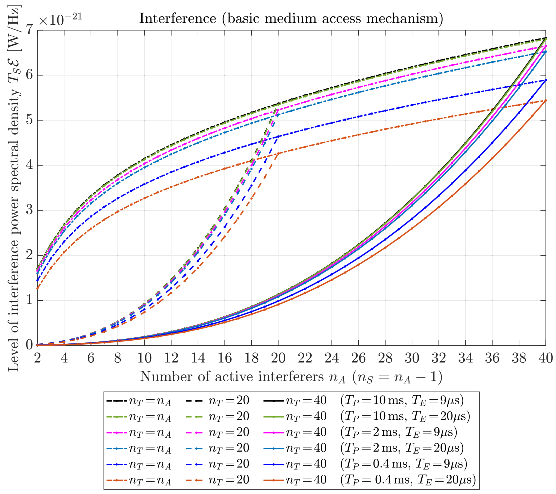

FIGURE 10. Interference PSD for the basic medium access mechanism, one access point, and up to forty devices within the Wi-Fi network, with an increasing number of those interfering with the reference receiver. For each setting, having all devices within the network interfering with the reference receiver presents the upper bound on the received interference (depicted by the dash-dotted line plots). For any fixed number of active interferers affecting the reference receiver, larger Wi-Fi networks produce less interference (as delineated by the solid-line and dashed-line plots).

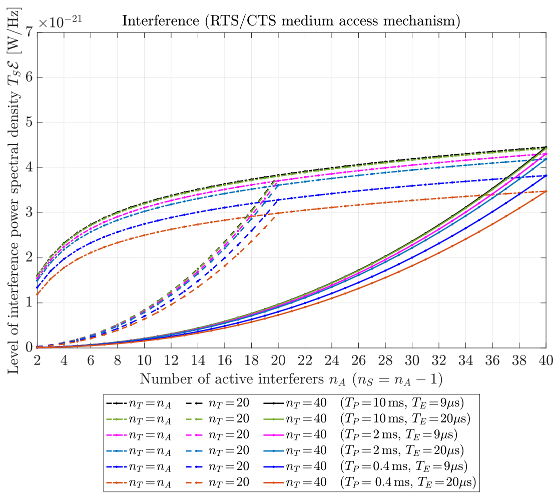

FIGURE 11. Interference PSD for the RTS/CTS medium access mechanism, one access point, and up to forty devices within the Wi-Fi network, with an increasing number of those interfering with the reference receiver. The considerations on the relative interference amount among different settings presented in Fig. 10 are still valid.

is as follows.

$$\mathrm{P_{pe}} = 1 - \prod_{\ell=0}^{n_s-1} \mathrm{P}_{\mathrm{sd}|\ell}. \tag{59}$$

From (11), (15), (44), and (45), we obtain (60), as shown at the bottom of the next page.

From (17), (48), and the definition of $\mathcal{W}(t)$,

$$\sum_{\mathtt{j}=\mathtt{I}}^{\mathtt{Q}} \left(\mathrm{W}^{\mathtt{j}}_{\ell|\mathtt{i}} - \mathrm{W}^{\mathtt{j}}_{\ell|\mathtt{l}}\right) \sim \mathcal{N}\left(0, \left(32 + \left|\varkappa^{\mathtt{II}}_{\mathtt{il}}\right| + \left|\varkappa^{\mathtt{QQ}}_{\mathtt{il}}\right|\right) N_0\right), \tag{61}$$

that is, the AWGN-related term has a normal distribution with zero mean and a specific variance.

From (18), the definitions of $\mathcal{V}_{u\iota}(t)$ and $\mathcal{V}_{d\iota}(t)$ as band-limited AWGN with variance $\sigma^2_{\mathcal{V}i}$ for each value i of ι, (53) taken together with (54) or (55), by the law of total probability and considerations from Section VIII-B, we obtain (62), as shown at the bottom of the next page. Note that the interference and noise terms in (60), expressed by (62) and (61), respectively, are statistically independent. Thus,

$$P\left(\mathrm{Z}_{\ell|\mathtt{il}} > 0\right) = \mathcal{Q}\left(\frac{-a_{\mathtt{il}}\hat{c}_t}{\sqrt{N_0 + T_s\mathcal{E}}}\right) = 1 - \mathcal{Q}\left(a_{\mathtt{il}}\sqrt{\hat{\gamma}_t}\right), \tag{63}$$

where $\mathcal{Q}(\cdot)$ indicates the Q-function [62, pp. 41 – 44] and

$$a_{\mathtt{il}} \triangleq \frac{32 - \varkappa^{\mathtt{II}}_{\mathtt{il}} - \varkappa^{\mathtt{QQ}}_{\mathtt{il}}}{\sqrt{32 + \left|\varkappa^{\mathtt{II}}_{\mathtt{il}}\right| + \left|\varkappa^{\mathtt{QQ}}_{\mathtt{il}}\right|}}. \tag{64}$$

From (10) and (63), the events in (58) are not independent because of the shared log-normal RV $\gamma(t)$. Therefore, we condition the events $\mathrm{Z}_{\ell|\mathtt{il}} > 0$ on $\gamma(t)$ with the same arbitrary value $\hat{\gamma}_t$ within its range to make them independent and find the following expression for the probability of PHY packet corruption:

$$\mathrm{P_{pe}}(\hat{\gamma}_t) = 1 - \left(\frac{1}{16}\sum_{\mathtt{i}=0}^{\mathtt{F}} \prod_{\mathtt{l}\neq\mathtt{i},\mathtt{l}=0}^{\mathtt{F}} \left(1 - \mathcal{Q}\left(a_{\mathtt{il}}\sqrt{\hat{\gamma}_t}\right)\right)\right)^{n_s}. \tag{65}$$

Fig. 12 shows $\mathrm{P_{pe}}(\hat{\gamma}_t)$ for varying amounts of control data transported in PHY packets of different sizes determined by related communication standards.

From (10) and the definition of the stochastic processes in Section VI-B, the probability density function (PDF) of the RV $\gamma(t)$ is

$$f_\gamma(\mathrm{x}) = \frac{1}{\mathrm{x}\sigma_\gamma\sqrt{2\pi}} e^{-\frac{\left(\ln(\mathrm{x}) - \mu_\gamma\right)^2}{2\sigma^2_\gamma}}, \tag{66}$$

where

$$\mu_\gamma = \mu_{\beta s} + 2\ln(\alpha_s) + \ln(E_c) - \ln(N_0 + T_s\mathcal{E}), \tag{67}$$

$$\sigma^2_\gamma = \sigma^2_{\beta s} + \sigma^2_\xi. \tag{68}$$

By the law of the unconscious statistician, the expected PER

$$\mu_{\mathrm{pe}} = \int_0^\infty \mathrm{P_{pe}}(\mathrm{x}) f_\gamma(\mathrm{x}) d\mathrm{x}. \tag{69}$$

Then, the PER variance is

$$\sigma^2_{\mathrm{pe}} = \int_0^\infty \mathrm{P}^2_{\mathrm{pe}}(\mathrm{x}) f_\gamma(\mathrm{x}) d\mathrm{x} - \mu^2_{\mathrm{pe}}. \tag{70}$$

Finally, note that the value $\hat{\gamma}_t$ of the RV $\gamma(t)$ is constant for the entire duration of the SoI frame and is observed via LQI or RSNI measurements on IEEE 802.15.4 receivers, as detailed in Section VI-B. The expected PER μ_{pe} in (69) and the PER variance σ^2_{pe} in (70) provide two important quality metrics for a specific channel of the LoI at a single transmission time scale. In the following, we show how our framework

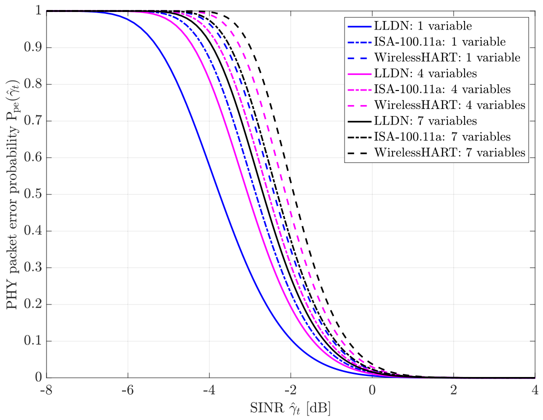

FIGURE 12. The PHY packet corruption probability in transporting 1, 4, or 7 sensing or actuation variables with LLDN, ISA-100, and WirelessHART communication standard.

Steps 2 and 3 in Fig. 4 guide the derivation of an accurate link model with the control application timing for the joint WNCS design.

D. MESSAGE ERROR PROBABILITY AND TEMPORAL CORRELATION

To derive a wireless link model suitable for control applications, we must inspect the selected sampling method, MAC scheme, channel-hopping mechanism, retransmission procedure, and node processing delay pattern. As outlined in Section II, we consider periodic communication between WNCS components with a definite sampling or publishing rate $\mathcal{R}$, depending on the control application requirements and wireless protocol characteristics. The highest supported rate is 100 Hz for IEEE 802.15.4e LLDNs and 10 Hz for WirelessHART-based implementations, whereas ISA-100.11a does not specify it. The ISA-100a standard describes only the 4 Hz (and slower) process monitoring structure, allowing multiple communication opportunities per cycle, which supports, for instance, compressor surge control loops running at 12 Hz cycle [51, Clause 9.1.9.1.3]. The case study we investigate concerns the TSCH MAC without retransmissions. Hence, there are no MAC-induced frame losses. The reference user connects to the access point directly via a single-hop link, thereby avoiding network-induced queuing delays, node-related network packet losses, and outdated message discarding. Therefore, the message error probability is equal to the PPDU dropout probability in (65).

If a WNCS has disabled channel-hopping, control-related transmissions occur every $\frac{1}{\mathcal{R}}$ s on the same radio channel. The stochastic process $\gamma(t)$ has the following autocovariance from the independence of the shadow fading of the PCE.

$$\rho_\gamma(\tau) = \rho_{\beta s}(\tau) + \rho_\xi(\tau), \tag{71}$$

where the right-hand-side addends are derived from (7) and (8). To evaluate the time correlations at the time scale of the control application, we must examine the autocovariance values for $\tau = \frac{k}{\mathcal{R}}$ with increasing positive integer k. The squared exponential structure of (71) induced by (7) and (8) implies that if $\rho_\gamma(\frac{k_1}{\mathcal{R}})=0$, then $\rho_\gamma(\frac{k_2}{\mathcal{R}})=0$ for any integer $k_2 > k_1$. Thus, obtaining $\rho_\gamma(\frac{1}{\mathcal{R}})=0$ indicates no time correlation between control-related transmissions. In contrast, $\rho_\gamma(\frac{1}{\mathcal{R}}) > 0$ and $\rho_\gamma(\frac{2}{\mathcal{R}}) = 0$ imply a correlation only between two consecutive transmissions, while having $\rho_\gamma(\frac{k}{\mathcal{R}}) > 0$ and $\rho_\gamma(\frac{k+1}{\mathcal{R}}) = 0$ suggests a correlation between $k+1$ control-related transmissions sent in sequence.

Note that a link of interest operates on different radio channels when channel-hopping is enabled. Nonetheless, the channel impairments presented in Section VI-B are the same for all considered channels in the ISM radio band. However, as described in Section VII, each IEEE 802.15.4 radio channel experiences different interference. Thus, each channel has a different mean expressed by (67) owing to the distinct values of $\mathcal{E}$ provided by (54) or (55). Instead, the variance (68) depends only on the channel impairments and has the same value for any channel in a hopping sequence. Consequently, the autocovariance function expression (71) also holds for the channel-hopping scenario with arbitrary hopping sequences, and the time correlation analysis presented above does not change.

IX. FINITE STATE LINK ABSTRACTION

A. STOCHASTIC FINITE-STATE LINK MODEL DERIVATION

The message error probability (65) characterizing the LoI in the considered scenario is a continuous function defined in the continuous domain of non-negative real numbers representing all possible SINR values. Thus, the LoI message dropout model has an infinite state space. However, the SINR estimation procedures implemented in IEEE 802.15.4-compliant receivers provide only a finite number of values, typically 255 or 256 [9, pp. 154–155, 457], so practical applications require using a finite number of channel and link states. The widely used FSMC model [85] divides an infinite

$$\mathrm{Z}_{\ell|\mathtt{i}\mathtt{l}} = \left(32 - \varkappa^{\mathtt{II}}_{\mathtt{il}} - \varkappa^{\mathtt{QQ}}_{\mathtt{il}}\right)\hat{c}_t + \sum_{\mathtt{j}=\mathtt{I}}^{\mathtt{Q}}\left(\mathrm{W}^{\mathtt{j}}_{\ell|\mathtt{i}} - \mathrm{W}^{\mathtt{j}}_{\ell|\mathtt{l}} + \sum_{\iota=0}^{n_\Upsilon+1}\left(\mathrm{V}^{\mathtt{j}}_{u\iota,\ell|\mathtt{i}} - \mathrm{V}^{\mathtt{j}}_{u\iota,\ell|\mathtt{l}} + \mathrm{V}^{\mathtt{j}}_{d\iota,\ell|\mathtt{i}} - \mathrm{V}^{\mathtt{j}}_{d\iota,\ell|\mathtt{l}}\right)\right). \tag{60}$$

$$\sum_{\mathtt{j}=\mathtt{I}}^{\mathtt{Q}}\sum_{\iota=0}^{n_\Upsilon+1}\left(\mathrm{V}^{\mathtt{j}}_{u\iota,\ell|\mathtt{i}} - \mathrm{V}^{\mathtt{j}}_{u\iota,\ell|\mathtt{l}} + \mathrm{V}^{\mathtt{j}}_{d\iota,\ell|\mathtt{i}} - \mathrm{V}^{\mathtt{j}}_{d\iota,\ell|\mathtt{l}}\right) \sim \mathcal{N}\left(0, \left(32+\left|\varkappa^{\mathtt{II}}_{\mathtt{il}}\right|+\left|\varkappa^{\mathtt{QQ}}_{\mathtt{il}}\right|\right)T_s\mathcal{E}\right), \tag{62}$$

range of SINR values into several consecutive regions, each associated with a specific representative message-error probability. This model maps region i of the SINR values delimited by two thresholds, $\hat{\mathrm{x}}_i$ and $\hat{\mathrm{x}}_{i+1}$, into a state $\mathbf{s}_i$ of the related Markov chain. The steady-state probability $\mathbf{p}_i$ of state $\mathbf{s}_i$ is the probability that the SINR lies between the region thresholds.

$$\mathbf{p}_i = \int_{\hat{\mathrm{x}}_i}^{\hat{\mathrm{x}}_{i+1}} f_\gamma(\mathrm{x}) d\mathrm{x}, \tag{72}$$

with (66) expressing the SINR PDF for an individual channel with a mean (67) and variance (68). We use the steady-state probability $\mathbf{p}_i$ to derive the message error probability of state $\mathbf{s}_i$ as the expected PER within the respective SINR region:

$$\mathrm{P}_{\mathrm{me}}^{(i)} = \frac{1}{\mathbf{p}_i} \int_{\hat{\mathrm{x}}_i}^{\hat{\mathrm{x}}_{i+1}} \mathrm{P}_{\mathrm{pe}}(\mathrm{x}) f_\gamma(\mathrm{x}) d\mathrm{x}. \tag{73}$$

Finally, by integrating the joint PDF of the SINR over two consecutive control-related transmissions and the desired regions, we obtain the FSMC state transition probabilities.

$$p_{ij} = \frac{\int_{\hat{\mathrm{x}}_i}^{\hat{\mathrm{x}}_{i+1}} \int_{\hat{\mathrm{x}}_j}^{\hat{\mathrm{x}}_{j+1}} f_\gamma(\mathrm{x}, \mathrm{y})\, d\mathrm{x} d\mathrm{y}}{\mathbf{p}_i}. \tag{74}$$

Note that (75), as shown at the bottom of the next page, is the relevant bivariate log-normal distribution for the FSMC model of the LoI without channel-hopping.

In a channel-hopping scenario, the LoI operates on different channels and switches between them following a predefined sequence. Thus, each radio channel has a specific steady-state probability. The channel-hopping sequence also induces transition probabilities between active radio channels. We denote the steady-state probability of a channel $\mathbf{c}_\imath$ within the hopping sequence by $\mathbf{q}_\imath$ and the transition probability between channels $\mathbf{c}_\imath$ and $\mathbf{c}_\jmath$ by $q_{\imath\jmath}$. Furthermore, we indicate the SINR PDF with the mean $\mu_{\gamma,\imath}$ of channel $\mathbf{c}_\imath$ as $f_{\gamma,\imath}(\mathrm{x})$. Recall that all channels within the hopping sequence have identical variances σ_γ^2 and autocovariance $\rho_\gamma(\tau)$. We can then derive an augmented FSMC model for the LoI. By substituting $f_\gamma(\mathrm{x})$ with $f_{\gamma,\imath}(\mathrm{x})$ in (72) and (73), we obtain the steady-state probabilities of the SINR regions and related message error probabilities for a given channel $\mathbf{c}_\imath$. In the slotted mode, IEEE 802.15.4-compliant devices use static hopping sequences [9, pp. 73 – 75] independent of the last measured SINR value. Consequently, the probability of transitioning from the SINR region $\left[\hat{\mathrm{x}}_i, \hat{\mathrm{x}}_{i+1}\right)$ on channel $\mathbf{c}_\imath$ to the SINR region $\left[\hat{\mathrm{x}}_j, \hat{\mathrm{x}}_{j+1}\right)$ on channel $\mathbf{c}_\jmath$ on the following control-related transmission is expressed by (76) and (77), as shown at the bottom of the next page.

$$p_{ij}^{\imath\jmath} = \frac{\int_{\hat{\mathrm{x}}_i}^{\hat{\mathrm{x}}_{i+1}} \int_{\hat{\mathrm{x}}_j}^{\hat{\mathrm{x}}_{j+1}} f_\gamma^\star(\mathrm{x}, \mathrm{y})\, d\mathrm{x} d\mathrm{y}}{\mathbf{q}_\imath \mathbf{p}_i}. \tag{76}$$

The values of the FSMC state transition probabilities obtained from (74) or (76) and the message error probabilities determined by (73) depend heavily on the choice of thresholds delimiting the SINR regions associated with each state. We set these thresholds systematically, as follows. Because the SINR values $\mathrm{x} \in [0, +\infty)$, any FSMC abstraction of a channel $\mathbf{c}_\imath$ with $n_\imath$ states has $\hat{\mathrm{x}}_1 = 0$ and $\hat{\mathrm{x}}_{n_\imath+1} = +\infty$. For any $n_\imath \geq 2$, we set the remaining SINR thresholds $\hat{\mathrm{x}}_i$, with $2 \leq i \leq n_\imath$, by a uniform partitioning of the message error probability range:

$$\hat{\mathrm{x}}_i \triangleq \min_{\mathrm{x}} \left(\mathrm{P}_{\mathrm{pe}}(\mathrm{x}) = \frac{i-1}{n_\imath} \right). \tag{78}$$

Note that (65) is a continuous monotonic non-increasing function of the SINR, and any standard root-finding algorithm provides the corresponding $\hat{\mathrm{x}}_i$ value. To assess the quality of the LoI and its finite-state abstraction, we derived the comprehensive quality metrics presented below.

B. LINK QUALITY METRICS

The first link quality metric (LQM) is the expected message error rate on a radio channel provided by (69) for the infinite-state analytical model considering the TSCH MAC without retransmissions. The corresponding metric for finite-state abstraction is the long-run mean message error probability, which, by construction, equals the expected message error rate on the same channel $\mathbf{c}_\imath$:

$$\mu_{\mathrm{me}}(\imath) = \sum_{i=1}^{n_\imath} \mathbf{p}_i(\imath) \mathrm{P}_{\mathrm{me}}^{(i)}(\imath) = \mu_{\mathrm{pe}}(\imath). \tag{79}$$

Similarly, the expected message error rate of the LoI with channel hopping among $1 \leq n_h \leq 16$ distinct radio channels equals the long-run mean message error probability:

$$\mu_{\mathrm{me}} = \sum_{\imath=1}^{n_h} \mathbf{q}_\imath \mu_{\mathrm{me}}(\imath) = \sum_{\imath=1}^{n_h} \mathbf{q}_\imath \mu_{\mathrm{pe}}(\imath) = \mu_{\mathrm{pe}}. \tag{80}$$

The first LQM indicates the value of the message dropout probability for the Bernoulli process, representing the coarsest abstraction of the LoI, which is accurate for scenarios without time correlation between control-related transmissions.

The second LQM of the infinite-state analytical model is the message error rate variance obtained for each radio channel via (70). The equivalent metric for FSMC abstraction is the long-run variance provided by the following expression:

$$\sigma_{\mathrm{me}}^2(\imath) = \sum_{i=1}^{n_\imath} \mathbf{p}_i(\imath) \Big(\mathrm{P}_{\mathrm{me}}^{(i)}(\imath)\Big)^2 - \mu_{\mathrm{me}}^2(\imath). \tag{81}$$

Note that increasing the number of channel states leads to FSMC abstraction with a long-run variance equal to the message error rate variance. Thus, the second LQM guides the selection of the number of states for FSMC abstraction to preserve the accuracy of the infinite-state model of the LoI with a perceivable fading correlation. According to the law of total variance, the message error rate variance and corresponding long-run variance of the link with channel hopping are provided by the same expression (82), as shown at the bottom of the next page, with $\mathrm{v} \in \{\mathrm{p}, \mathrm{m}\}$.

The third LQM is the maximum number of consecutive dropouts (MNCD, denoted by n_M), which is a parameter widely used in network control system design based on deterministic packet-dropout models [86], [87]. When there is no correlation among control-related transmissions, we have

$$n_M(\imath) = \left\lceil \frac{\ln\left(\frac{\epsilon}{1-\mu_{\mathrm{pe}}(\imath)}\right)}{\ln\left(\mu_{\mathrm{pe}}(\imath)\right)} \right\rceil, \tag{83}$$

where ϵ is a specified threshold, below which the likelihood of an event is negligible. The practical values of ϵ may be as small as those of machine epsilon. We derived (83) from (69) and (84), as shown at the bottom of the next page, by exploiting the fact that uncorrelated jointly normal RVs are independent. The same result can be obtained by analyzing the sojourn time [88] in the subset of states representing dropout events (labeled as zero) in a Markov chain modeling the transmission outcomes following a Bernoulli distribution. The approach based on sojourn-time analysis allows us to determine the MNCD in a setting with time correlation, where calculating the left-hand side of (84) may be computationally challenging, if not prohibitive. To find the MNCD in a radio channel $\mathbf{c}_\imath$ abstracted as an FSMC having $n_\imath$ states with message error probabilities $\mathrm{P}_{\mathrm{me}}^{(i)}$, we transform the FSMC into a Markov chain defined by the Cartesian product of the FSMC states and transmission outcomes. We label the states of successful transmissions as ones and message dropouts as zeros. Thus, we partition the state-space of the Markov chain of channel $\mathbf{c}_\imath$ into two subsets, $\mathbb{S}_1^\imath$ and $\mathbb{S}_0^\imath$. This partitioning decomposes the transition probability matrix $\mathbf{M}$ into four submatrices: $\mathbf{M} = \begin{bmatrix}\mathbf{M}_{00} & \mathbf{M}_{01}\\ \mathbf{M}_{10} & \mathbf{M}_{11}\end{bmatrix}$, where $\mathbf{M}_{00} = \mathbf{M}_{10} = \left[p_{ij}\mathrm{P}_{\mathrm{me}}^{(j)}(\imath)\right]_{i,j=1}^{n_\imath}$, and $\mathbf{M}_{01} = \mathbf{M}_{11} = \left[p_{ij}\left(1-\mathrm{P}_{\mathrm{me}}^{(j)}(\imath)\right)\right]_{i,j=1}^{n_\imath}$. The steady-state probability vector of the subset $\mathbb{S}_0^\imath$ is $\mathbf{m}_0 = \left[\mathbf{p}_i(\imath)\mathrm{P}_{\mathrm{me}}^{(j)}(\imath)\right]_{i=1}^{n_\imath}$. The probability of having k consecutive dropouts $\dagger$ is (85), as shown at the bottom of the next page, where $\mathbb{I}$ denotes the identity matrix of the appropriate size, $\mathbf{1}$ is the column vector of the appropriate length with all entries equal to the scalar one, and $^\top$ indicates the transpose. The MNBD is a solution to the optimization problem involving (85).

$$n_M(\imath) = \max_k \left(P(\dagger = k) > \epsilon\right). \tag{86}$$

Finding the MNCD via the presented sojourn time analysis is straightforward in scenarios with channel hopping because it only requires substituting the FSMC model of a radio channel with the augmented FSMC model of the LoI.

The following sections illustrate the use of the derived FSMC abstraction for the controller design in WNCS applications.

X. NETWORKED CONTROL

A. NETWORKED CONTROL SYSTEM ARCHITECTURE

Consider a linear stochastic system with intermittent control packets owing to a lossy communication channel [30].

$$x_{k+1} = \boldsymbol{A}x_k + \boldsymbol{B}u_k^a + w_k, \quad \text{with} \quad u_k^a = \nu_k u_k^c, \tag{87}$$

where $x_k \in \mathbb{R}^{n_x}$ is the system state, $u_k^a \in \mathbb{R}^{n_u}$ is the control input to the actuator, $\boldsymbol{A}$ and $\boldsymbol{B}$ are the state and input matrices of appropriate size, respectively, $u_k^c \in \mathbb{R}^{n_u}$ is the desired control input computed by the controller, and $w_k \in \mathbb{R}^{n_x}$ is the Gaussian white process noise with a zero mean and covariance matrix Σ_w. The process noise w_k is assumed to be independent from the initial state x_0 and of the stochastic variable ν_k, which models the packet loss between the controller and the actuator: if the packet is correctly delivered, then $u_k^a = u_k^c$; otherwise, if the packet is lost, the actuator does nothing, that is, $u_k^a = 0$. This scheme, known as the *zero-input dropout compensation* strategy [30], is summarized in (87).

We assume that the WNCS relies on a network protocol in which the sender receives ACKs of successful receptions within the same sampling period. We observe that the IEEE 802.15.4 protocols satisfy this assumption. To pinpoint the effects of the accuracy of the stochastic characterization of a packet loss process, we focus only on a radio link between the controller and actuators, thus assuming a full-state observation with no measurement noise and observation packet loss. The optimal control must be static state feedback;

$$f_\gamma(\mathrm{x},\mathrm{y}) = \frac{1}{2\pi\,\mathrm{xy}\sqrt{\sigma_\gamma^4 - \rho_\gamma^2(\frac{1}{\mathcal{R}})}} e^{-\frac{1}{2}\frac{\sigma_\gamma^2\left(\ln(\mathrm{x})-\mu_\gamma\right)^2 + \sigma_\gamma^2\left(\ln(\mathrm{y})-\mu_\gamma\right)^2 - 2\rho_\gamma(\frac{1}{\mathcal{R}})\left(\ln(\mathrm{x})-\mu_\gamma\right)\left(\ln(\mathrm{y})-\mu_\gamma\right)}{\sigma_\gamma^4 - \rho_\gamma^2(\frac{1}{\mathcal{R}})}}. \tag{75}$$

$$f_\gamma^\star(\mathrm{x},\mathrm{y}) = \frac{1}{2\pi\,\mathrm{xy}\sqrt{\sigma_\gamma^4 - \rho_\gamma^2(\frac{1}{\mathcal{R}})}} e^{-\frac{1}{2}\frac{\sigma_\gamma^2\left(\ln(\mathrm{x})-\mu_{\gamma,\imath}\right)^2 + \sigma_\gamma^2\left(\ln(\mathrm{y})-\mu_{\gamma,\jmath}\right)^2 - 2\rho_\gamma(\frac{1}{\mathcal{R}})\left(\ln(\mathrm{x})-\mu_{\gamma,\imath}\right)\left(\ln(\mathrm{y})-\mu_{\gamma,\jmath}\right)}{\sigma_\gamma^4 - \rho_\gamma^2(\frac{1}{\mathcal{R}})}}. \tag{77}$$

$$\sigma_{\mathrm{ve}}^2 = \sum_{\imath=1}^{n_h}\mathbf{q}_\imath\sigma_{\mathrm{ve}}^2(\imath) + \sum_{\imath=1}^{n_h}\mathbf{q}_\imath\left(1-\mathbf{q}_\imath\right)\mu_{\mathrm{ve}}^2(\imath) - 2\sum_{\imath=2}^{n_h}\sum_{\jmath=1}^{\imath-1}\mathbf{q}_\imath\mu_{\mathrm{ve}}(\imath)\mathbf{q}_\jmath\mu_{\mathrm{ve}}(\jmath). \tag{82}$$

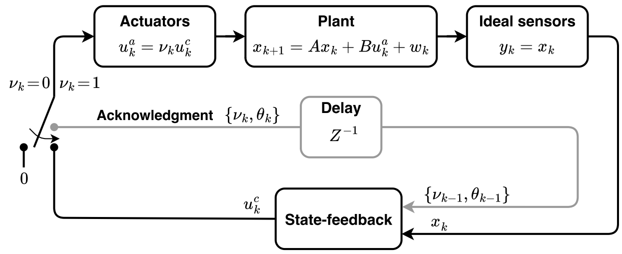

FIGURE 13. Architecture of the closed-loop system with state-feedback control input delivered to actuators over a wireless link. The binary random variable ν_k indicates the transmission outcome. The state θ_k of the link is measured for each received packet and fed back to the controller with either ACK or negative acknowledgment (N-ACK) signal.

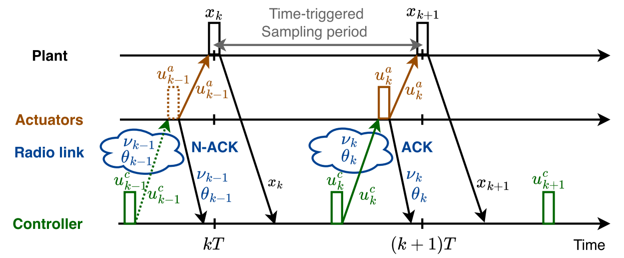

FIGURE 14. Timing diagram for a closed-loop system with time-triggered sampling and possible packet losses on a radio link between controller and actuators. In this example, at time step $k-1$, the control packet containing u_{k-1}^c is corrupted during the transmission. The receiver detects the error, discards the message and sends N-ACK signal stating that $\nu_{k-1} = 0$. The related packet contains the estimated state of the link, θ_{k-1}. At time step k, the control signal u_k^c is received correctly, so the ACK signal $\nu_k = 1$ is sent to the controller, together with the new estimation θ_k of the state of the link.

no filter is necessary. Fig. 13 and 14 show the architecture of the closed-loop system and the related timing diagram.

We aim to design an optimal infinite-horizon state-feedback control law that minimizes the performance index

$$J_\infty = \lim_{N\to\infty} \frac{1}{N}\,\mathbb{E}\left[\sum_{k=0}^{N} x_k^* \boldsymbol{Q} x_k + u_k^{a*} \boldsymbol{R} u_k^a\right], \tag{88}$$

where $\boldsymbol{Q} \succeq 0$ and $\boldsymbol{R} \succ 0$ are the state-weighting and control-weighting matrices, respectively. As in [30], we weight the control input to the actuator. When the desired control input u_k^c is not received, the actuator applies a zero input and has no energy expenditure.

The explicit form of the optimal control law that defines u_k^c depends on the stochastic properties of the packet loss process and information set available to the controller. In the following sections, to emphasize the impact of an accurate channel model in a networked control system, we consider two possible characterizations of the packet loss process, that is, Bernoulli and Markov processes, and define the corresponding optimal control law. We use the following stochastic stability notion: given a system (87) and a control law $u_k^c = K_{i(k)} x_k$, with $i(k) \le n_\iota$ indicating one of n_ι feedback gains, we say that the closed-loop system is *mean-square stable* if, for any x_0, $\lim_{k\to\infty} \mathbb{E}\left[x_k x_k'\right] = 0$, that is, the second moment of the system state asymptotically approaches zero.

B. CONTROL UNDER BERNOULLI PACKET LOSS

When control packet loss $\{\nu_k\}$ is a Bernoulli process, we have $\forall k$ that $P(\nu_k = 1) \triangleq \hat{\nu} = 1 - \mu_{\text{pe}}$. In this case, the information set available to the controller is

$$\mathcal{F}_k \triangleq \left\{\boldsymbol{x}^k, \boldsymbol{\nu}^{k-1}\right\}, \tag{89}$$

where $\boldsymbol{x}^k = (x_t)_{t=0}^k$ and $\boldsymbol{\nu}^k = (\nu_t)_{t=0}^k$ are the sequences of system states and control packet losses, respectively.

The optimal infinite-horizon state-feedback control law that minimizes (88) is given as a function of $\mathcal{F}_k$ as

$$u_k^{cB} = \boldsymbol{K} x_k = -\left(\boldsymbol{R} + \boldsymbol{B}^* \boldsymbol{X} \boldsymbol{B}\right)^{-1} \boldsymbol{B}^* \boldsymbol{X} \boldsymbol{A}\, x_k, \tag{90}$$

where the asterisk indicates the conjugate transpose, $\boldsymbol{X}$ is the unique positive semi-definite solution of the modified algebraic Riccati equation (MARE, [30]), and

$$\boldsymbol{X} = \boldsymbol{Q} + \boldsymbol{A}^* \boldsymbol{X} \boldsymbol{A} - \hat{\nu} \boldsymbol{A}^* \boldsymbol{X} \boldsymbol{B}\left(\boldsymbol{R} + \boldsymbol{B}^* \boldsymbol{X} \boldsymbol{B}\right)^{-1} \boldsymbol{B}^* \boldsymbol{X} \boldsymbol{A}. \tag{91}$$

If the state matrix $\boldsymbol{A}$ is unstable, pair $(\boldsymbol{A}, \boldsymbol{B})$ is controllable, and pair $\left(\boldsymbol{A}, \sqrt{\boldsymbol{Q}}\right)$ is observable, then solution $\boldsymbol{X}$ to (91) is stabilizing (in the mean square sense) if and only if $\hat{\nu} > \nu_c$ (see [30] together with [89]), where ν_c is the critical control packet arrival probability. Let $\lambda_i^u(\boldsymbol{A})$ denote the unstable eigenvalues of $\boldsymbol{A}$, and $|\cdot|$ denote the magnitude. The critical arrival probability ν_c satisfies

$$1 - \frac{1}{\max_i |\lambda_i^u(\boldsymbol{A})|^2} \le \nu_c \le 1 - \frac{1}{\prod_i |\lambda_i^u(\boldsymbol{A})|^2} \tag{92}$$

and can be computed numerically as the solution to a certain linear matrix inequality (LMI) optimization problem [30].

When the solution $\boldsymbol{X}$ to MARE is stabilizing, the optimal control law u_k^{cB} attains the optimal value of (88), which is

$$J_B = \operatorname{trace}(\boldsymbol{X}\Sigma_w). \tag{93}$$

$$\int_0^\infty \cdots \int_0^\infty \int_0^\infty \mathrm{P}_{\text{pe}}(\mathrm{x}_1) \cdots \mathrm{P}_{\text{pe}}(\mathrm{x}_{\mathrm{n_M}}) \left(1 - \mathrm{P}_{\text{pe}}(\mathrm{x}_{\mathrm{n_M}+1})\right) f_\gamma(\mathrm{x}_1, \ldots, \mathrm{x}_{n_M}, \mathrm{x}_{n_M+1}) d\mathrm{x}_1 \cdots d\mathrm{x}_{n_M} d\mathrm{x}_{n_M+1}$$
$$\stackrel{\perp\!\!\!\perp}{=} \int_0^\infty \mathrm{P}_{\text{pe}}(\mathrm{x}_1) f_\gamma(\mathrm{x}_1) d\mathrm{x}_1 \cdots \int_0^\infty \mathrm{P}_{\text{pe}}(\mathrm{x}_{\mathrm{n_M}}) f_\gamma(\mathrm{x}_{n_M}) d\mathrm{x}_{n_M} \int_0^\infty \left(1 - \mathrm{P}_{\text{pe}}(\mathrm{x}_{\mathrm{n_M}+1})\right) f_\gamma(\mathrm{x}_{n_M+1}) d\mathrm{x}_{n_M+1} < \epsilon. \tag{84}$$

$$P(\dagger = k) = \left(\mathbf{m}_0 \left(\mathbb{I} - \mathbf{M}_{00}\right) \mathbf{1}^\top\right)^{-1} \mathbf{m}_0 \left(\mathbb{I} - \mathbf{M}_{00}\right) \mathbf{M}_{00}^{k-1} \left(\mathbb{I} - \mathbf{M}_{00}\right) \mathbf{1}^\top. \tag{85}$$

C. CONTROL UNDER MARKOV CHANNEL PACKET LOSS

When the control packet loss process $\{\nu_k\}$ evolves according to the FSMC described in Section IX-A, the information set available to the controller is

$$\mathcal{G}_k = \left\{ \boldsymbol{x}^k, \boldsymbol{\nu}^{k-1}, \boldsymbol{\theta}^{k-1} \right\}, \tag{94}$$

where $\boldsymbol{\theta}^k = (\theta_t)_{t=0}^k$ is the sequence of measured link states. The probabilities of successful control packet delivery and packet loss depend on the state of the communication link, that is, $P(\nu_k = 1 \mid \theta_k = \mathbf{s}_i) \triangleq \hat{\nu}_i = 1 - \mathrm{P}_{\mathrm{me}}^{(i)}$, and $P(\nu_k = 0 \mid \theta_k = \mathbf{s}_i) \triangleq 1 - \hat{\nu}_i = \mathrm{P}_{\mathrm{me}}^{(i)}$. The WNCS behaves as a Markov jump linear system [90] with one time-step delayed mode observations and admits an optimal mode-dependent state-feedback controller [10]. The control law minimizing (88) according to (94) is (95), as shown at the bottom of the next page, where, for each operational mode $\mathbf{s}_i$, $\boldsymbol{Y}_i = \boldsymbol{Y}_i^*$ is the unique positive semi-definite solution to the coupled Riccati algebraic equations (96), as shown at the bottom of the next page. This solution stabilizes the WNCS (in the mean square sense) if and only if the spectral radius $\boldsymbol{\rho}$ of the characteristic matrix $\boldsymbol{\Lambda}$ defined by (97), as shown at the bottom of the next page, is smaller than one. In (97), the bar denotes conjugate, $\oplus$ indicates the horizontal concatenation of two matrices with the same number of rows, $\oplus$ designates the direct sum, and $\otimes$ means the Kronecker product. The mean-square stabilizing solution of (96) achieves the optimal value of the performance index (88):

$$J_M = \sum_{i=1}^{n_t} \mathbf{p}_i \mathrm{trace}(\boldsymbol{Y}_i \Sigma_w). \tag{98}$$

Note that if $\boldsymbol{\rho}(\boldsymbol{\Lambda}) < 1$ with $\boldsymbol{Y}_i = \boldsymbol{X}$ from (91) for all states $\mathbf{s}_i$, WNCS (87) admits a simpler mean-square stabilizing mode-independent control strategy that does not require knowledge of the channel state.

The following section illustrates the presented theoretical results on extensive numerical examples.

XI. PARAMETRIC ANALYSIS AND NUMERICAL EXAMPLES

To illustrate the impact of the interfering network on the wireless networked control performance, we consider an unstable system such as an inverted rotary pendulum controlled remotely through the link of interest presented in Section II. The controller aims to balance the pendulum in the upright vertical position corresponding to the inverted pendulum angle equal to zero. We use the pendulum model linearized around the unstable equilibrium point with parameters from [91] to obtain the following continuous-time system matrices:

$$\tilde{A} = \begin{bmatrix} 0 & 0 & 1 & 0 \\ 0 & 0 & 0 & 1 \\ 0 & 81.403 & -10.254 & -0.932 \\ 0 & 122.055 & -10.332 & -1.397 \end{bmatrix}, \quad \tilde{B} = \begin{bmatrix} 0 \\ 0 \\ 83.466 \\ 80.316 \end{bmatrix}.$$

TABLE 5. Link of interest propagation parameters.

Parameter	Value
$\sigma_{\beta s}$	3 dB
Δ_s	0.2 m
v_s	3 m/s
τ_ξ	$1.52 \cdot 10^{-3}$ s
σ_e	1.5 dB

The system state considers the rotary arm and pendulum angles and their derivatives, that is, the corresponding angular velocities. This linear model holds for small angles from the vertical, for instance, 10°, that is, 0.175 rad.

The controller is distant 5 m and transmits on channel 11 at 10 dBm. There are no obstacles between the controller and plant. Table 5 reports the remaining propagation environment parameters used in the analysis, and Table 3 lists the considered interfering network settings. We reuse the setup from Section VIII-B and examine the case of the RTS/CTS medium access mechanism and one access point among 40 devices within the Wi-Fi network generating interference PSD illustrated in Fig. 11. As before, all interfering devices are distant 10 m from the IEEE 802.15.4-compliant receiver and transmit at 10 dBm at channel one. We focus on a scenario with an empty IEEE 802.11n slot time $T_E = 20\,\mu$s and time to transmit a Wi-Fi PPDU $T_P = 10$ ms.

We examine the ISA-100.11a implementation with a sampling rate $\mathcal{R}$ of 12 Hz and the zero-order hold discretization method. The discrete-time system matrices are as follows.

$$\boldsymbol{A} = \begin{bmatrix} 1 & 0.224 & 0.055 & 0.004 \\ 0 & 1.369 & -0.028 & 0.090 \\ 0 & 4.994 & 0.391 & 0.167 \\ 0 & 8.618 & -0.634 & 1.270 \end{bmatrix}, \quad \boldsymbol{B} = \begin{bmatrix} 0.227 \\ 0.218 \\ 4.944 \\ 4.820 \end{bmatrix}.$$

Notably, the critical control packet arrival probability of this plant under the Bernoulli message loss is $\nu_c = 0.751$. For a system affected by Gaussian white process noise with covariance matrix $\Sigma_w = 2.5 \cdot 10^{-9}\,\mathbb{I}$, the considered system state weighting and control weighting matrices are

$$\boldsymbol{Q} = \begin{bmatrix} 1 & 0 & 0 & 0 \\ 0 & 5 & 0 & 0 \\ 0 & 0 & 1 & 0 \\ 0 & 0 & 0 & 1 \end{bmatrix}, \quad \boldsymbol{R} = 10.$$

For the receiver's noise temperature of 290 K, we analyze the performance of the infinite-horizon mode-independent and mode-dependent state-feedback control laws (90) and (95) in three cases corresponding to 16, 32, and 40 Wi-Fi devices affecting the link of interest. These three settings show different levels of control performance, with both control strategies successfully stabilizing the plant in the first case, both controllers failing to achieve their goals in the third case, and only the mode-dependent controller managing to stabilize the pendulum in the second case.

Before examining each case separately, we list their common characteristics. In all three cases, the expected SoI PSD in (56) is $\hat{c}_t^2 = 7.3 \cdot 10^{-20}$ W/Hz, AWGN PSD

$N_0 = 4 \cdot 10^{-21}$ W/Hz, SINR variance in (68) is $\sigma_\gamma^2 = 4.2$, and the relevant values of the SINR autocovariance from (71) are $\rho_\gamma(\frac{1}{\mathcal{R}}) = 1.823$, $\rho_\gamma(\frac{2}{\mathcal{R}}) = 0.175$, and $\rho_\gamma(\frac{3}{\mathcal{R}}) = 0.004$. As detailed in Section VIII-D, $\rho_\gamma(\frac{1}{\mathcal{R}}) > 0$ reveals the time correlation neglected by the Bernoulli packet loss model, and $\rho_\gamma(\frac{2}{\mathcal{R}}) > 0$ specifies the correlation between consecutive transmissions neglected by the FSMC model.

A. CASE 1: SIXTEEN INTERFERING DEVICES

Sixteen interfering Wi-Fi devices, including an access point, produce an interference PSD $T_s\mathcal{E} = 5.86 \cdot 10^{-22}$ W/Hz resulting in a nominal SINR $\hat{\gamma}_t$ in (56) of 15.9. The expected value of a log-normal SINR process defined by (67) is $\mu_\gamma = 2.766$, so the expected packet error rate in (69) is $\mu_{\text{pe}} = 0.051$, and the related PER variance in (70) is $\sigma_{\text{pe}}^2 = 0.041$.

With $\hat{\nu} = 1 - \mu_{\text{pe}} = 0.948 > \nu_c = 0.751$, the optimal Bernoulli gain from (90) is

$$\boldsymbol{K} = \begin{bmatrix} -0.065440 & 4.245749 & -0.281692 & 0.485146 \end{bmatrix},$$

and the Bernoullian control cost in (93) is $J_B = 3.6 \cdot 10^{-6}$.

A four-state Markov channel model with uniform partitioning of the message error probability range according to (78) has three thresholds corresponding to the SINR values of -3.21, -2.55, and -1.80 dB. The steady-state probability vector obtained from (72) is $\mathbf{p} = [0.042\ 0.007\ 0.009\ 0.942]$, the related packet error probability vector defined by (73) is $\mathrm{P_{me}} = [0.971\ 0.625\ 0.365\ 0.003]$, and the transition probability matrix computed using (74) is

$$\boldsymbol{P} = \begin{bmatrix} 0.195 & 0.024 & 0.028 & 0.753 \\ 0.137 & 0.019 & 0.024 & 0.820 \\ 0.129 & 0.018 & 0.023 & 0.830 \\ 0.034 & 0.006 & 0.008 & 0.952 \end{bmatrix}.$$

This FSMC has the following link quality metrics obtained from (79), (81), and (86), with $\imath = 11$: $\mu_{\text{me}} = 0.051$, $\sigma_{\text{me}}^2 = 0.041$, and $n_M = 23$ for $\epsilon = 2^{-52}$. In comparison, Bernoulli packet loss abstraction relies on (83) to obtain the maximum number of consecutive dropouts value of 13.

From (95), the optimal Markovian control gains are

$$\boldsymbol{L}_1 = \begin{bmatrix} -0.056116 & 4.323903 & -0.281949 & 0.488905 \end{bmatrix},$$
$$\boldsymbol{L}_2 = \begin{bmatrix} -0.056689 & 4.320547 & -0.281966 & 0.488758 \end{bmatrix},$$
$$\boldsymbol{L}_3 = \begin{bmatrix} -0.056781 & 4.320013 & -0.281968 & 0.488735 \end{bmatrix},$$
$$\boldsymbol{L}_4 = \begin{bmatrix} -0.057928 & 4.313297 & -0.282001 & 0.488442 \end{bmatrix},$$

and the Markovian control cost in (98) is $J_M = 4.8 \cdot 10^{-6}$.

Finally, from (97), we obtain $\boldsymbol{\rho}(\boldsymbol{\Lambda}) = 0.901$ for the Bernoulli control strategy and $\boldsymbol{\rho}(\boldsymbol{\Lambda}) = 0.908$ for the Markovian control strategy. Thus, the Bernoulli controller slightly outperforms the Markovian control strategy in the first case in terms of the speed of convergence, control cost, and complexity.

Section XI-D evaluates the differences in performance from 250000 Monte Carlo simulations with 90 s of balancing control. The following case instead shows that the Bernoulli controller performance severely degrades under heavier interference, with stronger oscillations resulting in an occasional loss of stability, whereas the Markovian controller continues to ensure stable behavior.

B. CASE 2: THIRTY TWO INTERFERING DEVICES

The interference PSD from 32 Wi-Fi devices is $T_s\mathcal{E} = 2.71 \cdot 10^{-21}$ W/Hz. It produces a nominal SINR $\hat{\gamma}_t$ in (56) of 10.86.

The expected value of a log-normal SINR process defined by (67) is $\mu_\gamma = 2.385$, the expected packet error rate in (69) is $\mu_{\text{pe}} = 0.074$, and the related PER variance in (70) is $\sigma_{\text{pe}}^2 = 0.059$. For $\hat{\nu} = 1 - \mu_{\text{pe}} = 0.926 > \nu_c = 0.751$, the optimal Bernoulli gain in (90) is

$$\boldsymbol{K} = \begin{bmatrix} -0.057023 & 4.354409 & -0.284374 & 0.492431 \end{bmatrix},$$

and the related control cost in (93) is $J_B = 4.98 \cdot 10^{-6}$. Since the expected packet arrival probability is well above the critical one and the expected control cost is relatively small, it would appear that the Bernoullian control strategy is appropriate.

The three SINR thresholds of an FSMC partitioned according to (78) are still -3.21, -2.55, and -1.80 dB. However, from (72), (73), and (74), the steady-state probability vector $\mathbf{p} = [0.061\ 0.010\ 0.012\ 0.917]$, packet error probability vector $\mathrm{P_{me}} = [0.973\ 0.625\ 0.366\ 0.004]$, and transition

$$u_k^{cM} = \boldsymbol{L}_{\theta_{k-1}} x_k = \left(\sum_{j=1}^{N} p_{ij}\hat{\nu}_j\left(\boldsymbol{B}^*\boldsymbol{Y}_j\boldsymbol{B}+\boldsymbol{R}\right)\right)^{-1}\left(\boldsymbol{A}^*\left(\sum_{j=1}^{N} p_{ij}\hat{\nu}_j\boldsymbol{Y}_j\right)\boldsymbol{B}\right)^* x_k \quad \text{for } \theta_{k-1} = \mathbf{s}_i. \tag{95}$$

$$\boldsymbol{Y}_i = \boldsymbol{A}^*\left(\sum_{j=1}^{N} p_{ij}\boldsymbol{Y}_j\right)\boldsymbol{A} + \boldsymbol{Q} - \left(\boldsymbol{A}^*\left(\sum_{j=1}^{N} p_{ij}\hat{\nu}_j\boldsymbol{Y}_j\right)\boldsymbol{B}\right)\left(\sum_{j=1}^{N} p_{ij}\hat{\nu}_j\left(\boldsymbol{B}^*\boldsymbol{Y}_j\boldsymbol{B}+\boldsymbol{R}\right)\right)^{-1}\left(\boldsymbol{A}^*\left(\sum_{j=1}^{N} p_{ij}\hat{\nu}_j\boldsymbol{Y}_j\right)\boldsymbol{B}\right)^*. \tag{96}$$

$$\boldsymbol{\Lambda} = \left(\bigoplus_{j=1}^{N}\left(\bigoplus_{i=1}^{N} p_{ij}\right)\right)^{\top} \otimes \left(\bigoplus_{j=1}^{N}(\bar{\boldsymbol{A}} \otimes \boldsymbol{A})\right) + \left(\bigoplus_{j=1}^{N}\left(\bigoplus_{i=1}^{N} \hat{\nu}_i p_{ij}\right)\right)^{\top} \otimes \left(\bigoplus_{j=1}^{N}\left(\left((\bar{\boldsymbol{B}}\bar{\boldsymbol{L}}_j) \otimes (\boldsymbol{B}\boldsymbol{L}_j)\right) + \left((\bar{\boldsymbol{B}}\bar{\boldsymbol{L}}_j) \otimes \boldsymbol{A}\right) + \left(\bar{\boldsymbol{A}} \otimes (\boldsymbol{B}\boldsymbol{L}_j)\right)\right)\right). \tag{97}$$

probability matrix

$$\boldsymbol{P} = \begin{bmatrix} 0.233 & 0.026 & 0.031 & 0.710 \\ 0.165 & 0.022 & 0.026 & 0.787 \\ 0.155 & 0.021 & 0.025 & 0.799 \\ 0.048 & 0.008 & 0.011 & 0.933 \end{bmatrix}.$$

The link quality metrics obtained from (79), (81), and (86) with $\imath = 11$ are $\mu_{\text{me}} = 0.074$, $\sigma^2_{\text{me}} = 0.058$, and $n_M = 26$ for $\epsilon = 2^{-52}$. From (83) with the same ϵ, the Bernoullian estimation of MNCD is 14.

The optimal Markovian control gains obtained via (95) are

$$\boldsymbol{L}_1 = \begin{bmatrix} -0.013786 & 4.544854 & -0.278523 & 0.496476 \end{bmatrix},$$
$$\boldsymbol{L}_2 = \begin{bmatrix} -0.014078 & 4.545229 & -0.278639 & 0.496587 \end{bmatrix},$$
$$\boldsymbol{L}_3 = \begin{bmatrix} -0.014123 & 4.545287 & -0.278657 & 0.496605 \end{bmatrix},$$
$$\boldsymbol{L}_4 = \begin{bmatrix} -0.014693 & 4.546017 & -0.278883 & 0.496822 \end{bmatrix},$$

and the Markovian control cost in (98) is $J_M = 81.64 \cdot 10^{-6}$.

From (97), the stability analysis of both control strategies reveals that $\boldsymbol{\rho}(\boldsymbol{\Lambda}) = 0.992$ for Markovian control and $\boldsymbol{\rho}(\boldsymbol{\Lambda}) = 1.004$ for Bernoullian controller. The Monte Carlo simulations of balancing control in Section XI-D demonstrate that the Bernoulli control strategy cannot ensure closed-loop stability, whereas the Markovian strategy stabilizes the system at the expense of complexity and average control cost.

C. CASE 3: FORTY INTERFERING DEVICES

When all devices in the interfering Wi-Fi network affect the link of interest, the interfering PSD $T_s\mathcal{E} = 4.43 \cdot 10^{-21}$ W/Hz, and a nominal SINR $\hat{\gamma}_t = 8.65$ in (56). From (67), (69), and (70), $\mu_\gamma = 2.158$, $\mu_{\text{pe}} = 0.091$, and $\sigma^2_{\text{pe}} = 0.071$.

With $\hat{\nu} = 1 - \mu_{\text{pe}} = 0.909$, which is still well above the critical threshold $\nu_c = 0.751$, the optimal Bernoulli gain in (90) is

$$\boldsymbol{K} = \begin{bmatrix} -0.048848 & 4.432010 & -0.285441 & 0.496926 \end{bmatrix},$$

and the optimal Bernoulli cost $J_B = 7.01 \cdot 10^{-6}$.

As before, the four-state Markov channel SINR thresholds are -3.21, -2.55, and -1.80 dB. From (72), (73), and (74), the values of the steady-state probability vector $\mathbf{p}$, packet error probability vector P_{me}, and transition probability matrix $\boldsymbol{P}$ are as follows: $\mathbf{p} = \begin{bmatrix} 0.076 \, 0.012 \, 0.014 \, 0.898 \end{bmatrix}$, while $\mathrm{P}_{\text{me}} = \begin{bmatrix} 0.974 \, 0.625 \, 0.366 \, 0.005 \end{bmatrix}$, and

$$\boldsymbol{P} = \begin{bmatrix} 0.257 & 0.027 & 0.032 & 0.684 \\ 0.182 & 0.023 & 0.028 & 0.767 \\ 0.172 & 0.022 & 0.027 & 0.779 \\ 0.058 & 0.010 & 0.012 & 0.920 \end{bmatrix}.$$

The related LQMs obtained from (79), (81), and (86) for $\imath = 11$ are $\mu_{\text{me}} = 0.091$, $\sigma^2_{\text{me}} = 0.071$, and $n_M = 28$ for $\epsilon = 2^{-52}$. From (83) with the same ϵ, the Bernoullian estimation of MNCD is 15.

From (95), the optimal Markovian control gains are

$$\boldsymbol{L}_1 = \begin{bmatrix} 0.000000 & 4.411655 & -0.275084 & 0.489338 \end{bmatrix},$$
$$\boldsymbol{L}_2 = \begin{bmatrix} 0.000000 & 4.350636 & -0.271526 & 0.483874 \end{bmatrix},$$
$$\boldsymbol{L}_3 = \begin{bmatrix} 0.000000 & 4.342384 & -0.271028 & 0.483119 \end{bmatrix},$$
$$\boldsymbol{L}_4 = \begin{bmatrix} 0.000000 & 4.252533 & -0.265354 & 0.474652 \end{bmatrix}.$$

The Markovian control cost in (98) is huge: $J_M = 6.21 \cdot 10^{11}$.

From (97), the stability analysis reveals that $\boldsymbol{\rho}(\boldsymbol{\Lambda}) = 1.089$ for mode-dependent Markovian control and $\boldsymbol{\rho}(\boldsymbol{\Lambda}) = 1.095$ for Bernoullian control. In this case, the recursive solution of the coupled difference Riccati equations does not converge, and the related Markov jump system is unstable.

The following section indeed shows that neither control strategy stabilizes the plant.

D. CONTROL PERFORMANCE EVALUATION

To validate the results of the previous sections, we performed 250000 Monte Carlo simulations of the closed-loop balancing control of the presented inverted rotary pendulum under the Markovian and Bernoullian control strategies. We generated 250000 independent realizations of the process noise for each scenario with $\frac{1}{12}$ s sampling time and a covariance matrix $\Sigma_w = 2.5 \cdot 10^{-9}\,\mathbb{I}$. Each trace lasted 90 s and registered channel-state evolution and successful control packet arrivals. We applied Markovian and Bernoullian control strategies to the same traces to obtain the closed-loop evolution of the plant's states starting from the unstable equilibrium point $x_0 = \begin{bmatrix} 0\,0\,0\,0 \end{bmatrix}$. The results are shown in Fig. 15. The solid lines show the extreme behavior in each considered case; thus, each system state evolution lies in the shaded area within the boundaries delineated by the observed extreme behavior. The green color in Fig. 15 identifies the first case, which is characterized by 16 active interfering devices. The observed behavior is almost indistinguishable between the two control strategies. Computing finite-horizon performance index

$$J_N = \sum_{k=0}^{N} \left(x_k^* \boldsymbol{Q} x_k + u_k^{a*} \boldsymbol{R} u_k^a \right), \tag{99}$$

where $N = 90 \cdot 12 = 1080$ is the number of samples in each trace, shows that the average cost is $J^{B,1}_{N,\text{avg}} = 0.004830$ under Bernoullian control and $J^{M,1}_{N,\text{avg}} = 0.004835$ under Markovian control. The maximal observed costs are $J^{B,1}_{N,\max} = 39.468$ for the Bernoullian strategy and $J^{M,1}_{N,\max} = 40.648$ for the Markovian strategy. Consequently, applying Bernoullian control to the inverted rotary pendulum offers lower complexity and slightly better performance when the remotely controlled system is strongly mean-square stabilizable, that is, when the mode-independent control strategy satisfies the stability condition $\boldsymbol{\rho}(\boldsymbol{\Lambda}) < 1$ for $\boldsymbol{\Lambda}$ defined by (97) with $\boldsymbol{L}_j = \boldsymbol{K}$ for all states $\mathbf{s}_j$. The violet color in Fig. 15 indicates the second case, which corresponds to a scenario with 32 actively interfering devices. The Markovian control strategy on the left-hand side of the figure exhibits slower movements of the rotary arm, which is characterized by milder slopes and lighter pendulum oscillations. By contrast, the Bernoulli controller produces faster rotary arm movements and much

FIGURE 15. **The inverted rotary pendulum state evolution in three cases corresponding to 16, 32, and 40 devices actively interfering with the link of interest. The solid lines emphasize the observed extreme behavior, so all the traces of each case lie within a shaded area delimited by the solid lines.**

stronger oscillations, which may result in a loss of stability. For instance, just after the 61 s mark, the pendulum angle on the right-hand side of Fig. 15 is at the boundary of the model linearization region (with a value of -0.18 rad), where the linear model used for the controller design starts to lose its validity. The finite-horizon performance index (99) analysis reveals that the average cost of the Bernoulli control $J^{B,2}_{N,\mathrm{avg}} = 0.009432$ is slightly lower than the average Markovian control cost $J^{M,2}_{N,\mathrm{avg}} = 0.011028$. However, the maximal observed Bernoullian cost is more than double that of the first scenario, with $J^{B,2}_{N,\max} = 82.390852$. This is considerably more significant than the maximal observed cost of the Markovian control, $J^{M,1}_{N,\max} = 47.874737$, whose growth compared to the first scenario remained moderate. Finally, the red color in Fig. 15 marks the third case of all 40 devices within a Wi-Fi network interfering with the link of interest. The pendulum oscillations become more pronounced than in the second case, with the angle approaching the -0.38 rad value, which is outside the model linearization region, just after the 21 s mark under the Bernoullian control strategy. Rotary arm movements become even faster, and the Markovian controller occasionally fails to bring the rotary arm to the desired position. The finite-horizon performance index (99) analysis highlights a severe performance degradation, with the average and maximal observed costs of Bernoullian and Markovian control becoming $J^{B,3}_{N,\mathrm{avg}} = 0.019048$, $J^{M,3}_{N,\mathrm{avg}} = 0.092353$, $J^{B,3}_{N,\max} = 387.526157$, and $J^{M,3}_{N,\max} = 584.262494$, respectively.

The presented control performance analysis highlights the importance of accurate communication link models for co-designing wireless networked control systems. Our study shows that neglecting the temporal correlation properties may lead to drastic performance degradation and even stability loss, even in scenarios in which the average control packet arrival probability is well above the critical threshold defined for the Bernoulli message dropout model.

XII. CONCLUSION

This study addressed the need for a detailed and flexible WNCS co-design approach. It thoroughly analyzed message dropout dependencies, illustrated the complexity of the interplay between the control and communication subsystems, and proposed a framework for co-designing delay-sensitive WNCSs using a four-step implementation procedure. As a case study demonstrating the proposed framework, we investigated the coexistence of two wireless networks and the performance of wireless control that relies on one of them. We derived analytical expressions for the interference power spectral density and control message error probability and examined their impact on the wireless feedback control performance in terms of mean-square stability and control cost. We also discussed the influence of temporal correlation on a control-level time scale and developed a corresponding finite-state Markov channel model of the wireless link together with quality metrics to assess the correctness of the proposed model.

Through extensive parametric analysis and Monte Carlo simulations, we verified that the coarsest link abstraction via the Bernoulli message loss process is suitable not only for scenarios without time correlation between control-related transmissions but also for time-correlated scenarios with plants that allow for a mode-independent mean-square stabilizing control strategy. Conversely, harsh propagation environments and substantial interference may not allow mode-independent control. Thus, constructing an accurate finite-state Markov channel model is vital for verifying the stability of the closed-loop control and choosing an appropriate control strategy. Indeed, the critical control packet arrival probability under Bernoulli message loss fails to capture the unstable behavior in a time-correlated setting.

REFERENCES

[1] E. Sisinni, A. Saifullah, S. Han, U. Jennehag, and M. Gidlund, "Industrial Internet of Things: Challenges, opportunities, and directions," *IEEE Trans. Ind. Informat.*, vol. 14, no. 11, pp. 4724–4734, Nov. 2018.

[2] W. Mao, Z. Zhao, Z. Chang, G. Min, and W. Gao, "Energy-efficient Industrial Internet of Things: Overview and open issues," *IEEE Trans. Ind. Informat.*, vol. 17, no. 11, pp. 7225–7237, Nov. 2021.

[3] W. Liu, P. Popovski, Y. Li, and B. Vucetic, "Wireless networked control systems with coding-free data transmission for industrial IoT," *IEEE Internet Things J.*, vol. 7, no. 3, pp. 1788–1801, Mar. 2020.

[4] M. Eisen, M. M. Rashid, K. Gatsis, D. Cavalcanti, N. Himayat, and A. Ribeiro, "Control aware radio resource allocation in low latency wireless control systems," *IEEE Internet Things J.*, vol. 6, no. 5, pp. 7878–7890, Oct. 2019.

[5] K. Huang, W. Liu, Y. Li, A. Savkin, and B. Vucetic, "Wireless feedback control with variable packet length for industrial IoT," *IEEE Wireless Commun. Lett.*, vol. 9, no. 9, pp. 1586–1590, Sep. 2020.

[6] W. Liu, G. Nair, Y. Li, D. Nesic, B. Vucetic, and H. V. Poor, "On the latency, rate, and reliability tradeoff in wireless networked control systems for IIoT," *IEEE Internet Things J.*, vol. 8, no. 2, pp. 723–733, Jan. 2021.

[7] P. Park, S. C. Ergen, C. Fischione, C. Lu, and K. H. Johansson, "Wireless network design for control systems: A survey," *IEEE Commun. Surveys Tuts.*, vol. 20, no. 2, pp. 978–1013, 2nd Quart., 2018.

[8] C. Lu, A. Saifullah, B. Li, M. Sha, H. Gonzalez, D. Gunatilaka, C. Wu, L. Nie, and Y. Chen, "Real-time wireless sensor-actuator networks for industrial cyber-physical systems," *Proc. IEEE*, vol. 104, no. 5, pp. 1013–1024, May 2016.

[9] *IEEE Standard for Low-Rate Wireless Networks*, IEEE Standard 802.15.4-2020, 2020.

[10] Y. Zacchia Lun and A. D'Innocenzo, "Stabilizability of Markov jump linear systems modeling wireless networked control scenarios," in *Proc. IEEE 58th Conf. Decis. Control (CDC)*, Dec. 2019, pp. 5766–5772.

[11] Y. Cheng, D. Yang, H. Zhou, and H. Wang, "Adopting IEEE 802.11 MAC for industrial delay-sensitive wireless control and monitoring applications: A survey," *Comput. Netw.*, vol. 157, pp. 41–67, Jul. 2019.

[12] F. Tramarin, S. Vitturi, M. Luvisotto, and A. Zanella, "On the use of IEEE 802.11n for industrial communications," *IEEE Trans. Ind. Informat.*, vol. 12, no. 5, pp. 1877–1886, Oct. 2016.

[13] S. Y. Shin, H. S. Park, S. Choi, and W. H. Kwon, "Packet error rate analysis of ZigBee under WLAN and Bluetooth interferences," *IEEE Trans. Wireless Commun.*, vol. 6, no. 8, pp. 2825–2830, Aug. 2007.

[14] G. Yang and Y. Yu, "ZigBee networks performance under WLAN 802.11b/g interference," in *Proc. 4th Int. Symp. Wireless Pervasive Comput.*, Feb. 2009, pp. 1–4.

[15] I. Tinnirello, G. Bianchi, and Y. Xiao, "Refinements on IEEE 802.11 distributed coordination function modeling approaches," *IEEE Trans. Veh. Technol.*, vol. 59, no. 3, pp. 1055–1067, Mar. 2010.

[16] D. Yang, Y. Xu, and M. Gidlund, "Wireless coexistence between IEEE 802.11- and IEEE 802.15.4-based networks: A survey," *Int. J. Distrib. Sensor Netw.*, vol. 7, no. 1, Jan. 2011, Art. no. 912152.

[17] D. Chen, Y. Zhuang, J. Huai, X. Sun, X. Yang, M. A. Javed, J. Brown, Z. Sheng, and J. Thompson, "Coexistence and interference mitigation for WPANs and WLANs from traditional approaches to deep learning: A review," *IEEE Sensors J.*, vol. 21, no. 22, pp. 25561–25589, Nov. 2021.

[18] A. Merwaday, R. Vannithamby, M. Eisen, S. Sudhakaran, D. A. Cavalcanti, and V. Frascolla, "Communication-control co-design for robotic manipulation in 5G industrial IoT," in *Proc. IEEE 21st Int. Conf. Ind. Informat. (INDIN)*, Jul. 2023, pp. 1–6.

[19] X. Ling, Y. Cheng, J. W. Mark, and X. Shen, "A renewal theory based analytical model for the contention access period of IEEE 802.15.4 MAC," *IEEE Trans. Wireless Commun.*, vol. 7, no. 6, pp. 2340–2349, Jun. 2008.

[20] P. Di Marco, P. Park, C. Fischione, and K. H. Johansson, "Analytical modeling of multi-hop IEEE 802.15.4 networks," *IEEE Trans. Veh. Technol.*, vol. 61, no. 7, pp. 3191–3208, Sep. 2012.

[21] X. Cao, J. Chen, Y. Cheng, X. S. Shen, and Y. Sun, "An analytical MAC model for IEEE 802.15.4 enabled wireless networks with periodic traffic," *IEEE Trans. Wireless Commun.*, vol. 14, no. 10, pp. 5261–5273, Oct. 2015.

[22] D. De Guglielmo, F. Restuccia, G. Anastasi, M. Conti, and S. K. Das, "Accurate and efficient modeling of 802.15.4 unslotted CSMA/CA through event chains computation," *IEEE Trans. Mobile Comput.*, vol. 15, no. 12, pp. 2954–2968, Dec. 2016.

[23] C.-H. Wang, C.-T. Chou, P. Lin, and M. Guizani, "Performance evaluation of IEEE 802.15.4 nonbeacon-enabled mode for Internet of Vehicles," *IEEE Trans. Intell. Transp. Syst.*, vol. 16, no. 6, pp. 3150–3159, Dec. 2015.

[24] S. Biswas, S. D. Roy, and A. Chandra, "Cross-layer energy model for non-beacon-enabled IEEE 802.15.4 networks," *IEEE Wireless Commun. Lett.*, vol. 9, no. 7, pp. 1084–1088, Jul. 2020.

[25] C. Gezer, A. Zanella, and R. Verdone, "An analytical model for the performance analysis of concurrent transmission in IEEE 802.15.4," *Sensors*, vol. 14, no. 3, pp. 5622–5643, Mar. 2014.

[26] M. Wilhelm, V. Lenders, and J. B. Schmitt, "On the reception of concurrent transmissions in wireless sensor networks," *IEEE Trans. Wireless Commun.*, vol. 13, no. 12, pp. 6756–6767, Dec. 2014.

[27] T. Hayajneh, G. Almashaqbeh, S. Ullah, and A. V. Vasilakos, "A survey of wireless technologies coexistence in WBAN: Analysis and open research issues," *Wireless Netw.*, vol. 20, no. 8, pp. 2165–2199, Nov. 2014.

[28] A. M. Mamadou, J. Toussaint, and G. Chalhoub, "Survey on wireless networks coexistence: Resource sharing in the 5G era," *Mobile Netw. Appl.*, vol. 25, no. 5, pp. 1749–1764, Oct. 2020.

[29] D. Baumann, F. Mager, U. Wetzker, L. Thiele, M. Zimmerling, and S. Trimpe, "Wireless control for smart manufacturing: Recent approaches and open challenges," *Proc. IEEE*, vol. 109, no. 4, pp. 441–467, Apr. 2021.

[30] L. Schenato, B. Sinopoli, M. Franceschetti, K. Poolla, and S. S. Sastry, "Foundations of control and estimation over lossy networks," *Proc. IEEE*, vol. 95, no. 1, pp. 163–187, Jan. 2007.

[31] A. Impicciatore, Y. Zacchia Lun, P. Pepe, and A. D'Innocenzo, "Optimal output-feedback control and separation principle for Markov jump linear systems modeling wireless networked control scenarios," in *Proc. Amer. Control Conf. (ACC)*, May 2021, pp. 2700–2706.

[32] A. Impicciatore, Y. Zacchia Lun, P. Pepe, and A. D'Innocenzo, "Optimal output-feedback control over Markov wireless communication channels," *IEEE Trans. Autom. Control*, vol. 69, no. 3, pp. 1643–1658, Mar. 2024.

[33] A. S. Leong, S. Dey, and D. E. Quevedo, "Transmission scheduling for remote state estimation and control with an energy harvesting sensor," *Automatica*, vol. 91, pp. 54–60, May 2018.

[34] A. S. Leong, A. Ramaswamy, D. E. Quevedo, H. Karl, and L. Shi, "Deep reinforcement learning for wireless sensor scheduling in cyber–physical systems," *Automatica*, vol. 113, Mar. 2020, Art. no. 108759.

[35] Y. Ma, J. Guo, Y. Wang, A. Chakrabarty, H. Ahn, P. Orlik, X. Guan, and C. Lu, "Optimal dynamic transmission scheduling for wireless networked control systems," *IEEE Trans. Control Syst. Technol.*, vol. 30, no. 6, pp. 2360–2376, Nov. 2022.

[36] K. Gatsis, H. Hassani, and G. J. Pappas, "Latency-reliability tradeoffs for state estimation," *IEEE Trans. Autom. Control*, vol. 66, no. 3, pp. 1009–1023, Mar. 2021.

[37] Y. Li, D. E. Quevedo, S. Dey, and L. Shi, "SINR-based DoS attack on remote state estimation: A game-theoretic approach," *IEEE Trans. Control Netw. Syst.*, vol. 4, no. 3, pp. 632–642, Sep. 2017.

[38] Z. Guo, D. Shi, K. H. Johansson, and L. Shi, "Optimal linear cyber-attack on remote state estimation," *IEEE Trans. Control Netw. Syst.*, vol. 4, no. 1, pp. 4–13, Mar. 2017.

[39] A. Tsiamis, K. Gatsis, and G. J. Pappas, "State-secrecy codes for networked linear systems," *IEEE Trans. Autom. Control*, vol. 65, no. 5, pp. 2001–2015, May 2020.
[40] A. S. Leong, D. E. Quevedo, D. Dolz, and S. Dey, "Information bounds for state estimation in the presence of an eavesdropper," *IEEE Control Syst. Lett.*, vol. 3, no. 3, pp. 547–552, Jul. 2019.
[41] A. Impicciatore, A. Tsiamis, Y. Zacchia Lun, A. D'Innocenzo, and G. J. Pappas, "Secure state estimation over Markov wireless communication channels," in *Proc. IEEE 61st Conf. Decis. Control (CDC)*, Dec. 2022, pp. 2935–2940.
[42] B. Chang, G. Zhao, L. Zhang, M. A. Imran, Z. Chen, and L. Li, "Dynamic communication QoS design for real-time wireless control systems," *IEEE Sensors J.*, vol. 20, no. 6, pp. 3005–3015, Mar. 2020.
[43] M. Eisen, S. Shukla, D. Cavalcanti, and A. S. Baxi, "Communication-control co-design in wireless edge industrial systems," in *Proc. IEEE 18th Int. Conf. Factory Commun. Syst. (WFCS)*, Apr. 2022, pp. 1–8.
[44] X. Tong, G. Zhao, M. A. Imran, Z. Pang, and Z. Chen, "Minimizing wireless resource consumption for packetized predictive control in real-time cyber physical systems," in *Proc. IEEE Int. Conf. Commun. Workshops (ICC Workshops)*, May 2018, pp. 1–6.
[45] P. K. Mishra, D. Chatterjee, and D. E. Quevedo, "Stochastic predictive control under intermittent observations and unreliable actions," *Automatica*, vol. 118, Aug. 2020, Art. no. 109012.
[46] A. M. Girgis, J. Park, M. Bennis, and M. Debbah, "Predictive control and communication co-design via two-way Gaussian process regression and AoI-aware scheduling," *IEEE Trans. Commun.*, vol. 69, no. 10, pp. 7077–7093, Oct. 2021.
[47] S. Yan, M. Cannon, and P. J. Goulart, "Stochastic output feedback MPC with intermittent observations," *Automatica*, vol. 141, Jul. 2022, Art. no. 110282.
[48] W. P. M. H. Heemels, K. H. Johansson, and P. Tabuada, "An introduction to event-triggered and self-triggered control," in *Proc. IEEE 51st IEEE Conf. Decis. Control (CDC)*, Dec. 2012, pp. 3270–3285.
[49] K. You, W. Su, M. Fu, and L. Xie, "Attainability of the minimum data rate for stabilization of linear systems via logarithmic quantization," *Automatica*, vol. 47, no. 1, pp. 170–176, Jan. 2011.
[50] *Industrial Communication Networks—Fieldbus Specifications—Part 1: Overview and Guidance for the IEC 61158 and IEC 61784 Series*, IEC Standard 61158-1:2019, 2019.
[51] *Industrial Networks—Wireless Communication Network and Communication Profiles—ISA 100.11a*, IEC Standard 62734:2014, 2014.
[52] J. L. Jerez, P. J. Goulart, S. Richter, G. A. Constantinides, E. C. Kerrigan, and M. Morari, "Embedded predictive control on an FPGA using the fast gradient method," in *Proc. Eur. Control Conf. (ECC)*, Jul. 2013, pp. 3614–3620.
[53] J. Xiong and J. Lam, "Stabilization of networked control systems with a logic ZOH," *IEEE Trans. Autom. Control*, vol. 54, no. 2, pp. 358–363, Feb. 2009.
[54] A. Grami, *Introduction to Digital Communications*. New York, NY, USA: Academic, 2015.
[55] *IEEE Standard for Information Technology—Telecommunications and Information Exchange Between Systems—Local and Metropolitan Area Networks—Specific Requirements—Part 11: Wireless LAN Medium Access Control (MAC) and Physical Layer (PHY) Specifications*, IEEE Standard 802.11-2020, 2020.
[56] I. B. F. de Almeida, M. Chafii, A. Nimr, and G. Fettweis, "Alternative chirp spread spectrum techniques for LPWANs," *IEEE Trans. Green Commun. Netw.*, vol. 5, no. 4, pp. 1846–1855, Dec. 2021.
[57] S. Lin and D. Costello Jr., *Error Control Coding*, 2nd ed. London, U.K.: Pearson, 2004.
[58] K. Jamieson and H. Balakrishnan, "PPR: Partial packet recovery for wireless networks," *ACM SIGCOMM Comput. Commun. Rev.*, vol. 37, no. 4, pp. 409–420, 2007.
[59] T. Watteyne, S. Lanzisera, A. Mehta, and K. S. J. Pister, "Mitigating multipath fading through channel hopping in wireless sensor networks," in *Proc. IEEE Int. Conf. Commun.*, May 2010, pp. 1–5.
[60] S. Dai, H. Qian, K. Kang, and W. Xiang, "A robust demodulator for OQPSK-DSSS system," *Circuits, Syst., Signal Process.*, vol. 34, no. 1, pp. 231–247, Jan. 2015.
[61] M. A. Zubair, A. K. Nain, J. Bandaru, P. Rajalakshmi, and U. B. Desai, "Reconfigurable dual mode IEEE 802.15.4 digital baseband receiver for diverse IoT applications," in *Proc. IEEE 3rd World Forum Internet Things (WF-IoT)*, Dec. 2016, pp. 389–394.
[62] J. G. Proakis and M. Salehi, *Digital Communications*, 5th ed. New York, NY, USA: McGraw-Hill, 2007.
[63] T. Vayssade, F. Azaïs, L. Latorre, and F. Lefèvre, "Low-cost digital test solution for symbol error detection of RF ZigBee transmitters," *IEEE Trans. Device Mater. Rel.*, vol. 19, no. 1, pp. 16–24, Mar. 2019.
[64] A. Goldsmith, *Wireless Communications*. Cambridge, U.K.: Cambridge Univ. Press, 2005.
[65] F. Barac, M. Gidlund, and T. Zhang, "Scrutinizing bit- and symbol-errors of IEEE 802.15.4 communication in industrial environments," *IEEE Trans. Instrum. Meas.*, vol. 63, no. 7, pp. 1783–1794, Jul. 2014.
[66] G. L. Stüber, *Principles of Mobile Communication*, 4th ed. Cham, Switzerland: Springer, 2017.
[67] *Coexistence Analysis of IEEE Std 802.15.4 With Other IEEE Standards and Proposed Standards*, document September, 2010 IEEE P802.15-10-0808-00, 2010.
[68] M. Damsaz, D. Guo, J. Peil, W. Stark, N. Moayeri, and R. Candell, "Channel modeling and performance of ZigBee radios in an industrial environment," in *Proc. IEEE 13th Int. Workshop Factory Commun. Syst. (WFCS)*, May 2017, pp. 1–10.
[69] T. S. Rappaport, Y. Xing, G. R. MacCartney, A. F. Molisch, E. Mellios, and J. Zhang, "Overview of millimeter wave communications for fifth-generation (5G) wireless networks—With a focus on propagation models," *IEEE Trans. Antennas Propag.*, vol. 65, no. 12, pp. 6213–6230, Dec. 2017.
[70] H. Kdouh, G. Zaharia, C. Brousseau, G. E. Zein, and G. Grunfelder, "ZigBee-based sensor network for shipboard environments," in *Proc. Int. Symp. Signals, Circuits Syst. (ISSCS)*, Jun. 2011, pp. 1–4.
[71] A. F. Molisch, "Ultrawideband propagation channels-theory, measurement, and modeling," *IEEE Trans. Veh. Technol.*, vol. 54, no. 5, pp. 1528–1545, Sep. 2005.
[72] N. Jalden, P. Zetterberg, B. Ottersten, A. Hong, and R. Thoma, "Correlation properties of large scale fading based on indoor measurements," in *Proc. IEEE Wireless Commun. Netw. Conf.*, Mar. 2007, pp. 1894–1899.
[73] A. Seetharam, J. Kurose, D. Goeckel, and G. Bhanage, "A Markov chain model for coarse timescale channel variation in an 802.16e wireless network," in *Proc. IEEE Conf. Comput. Commun. (INFOCOM)*, Mar. 2012, pp. 1800–1807.
[74] F. Graziosi, L. Fuciarelli, and E. Santucci, "Second order statistics of the SIR for cellular mobile networks in the presence of correlated co-channel interferers," in *Proc. IEEE VTS 53rd Veh. Technol. Conf.*, Spring 2001, pp. 2499–2503.
[75] Y. Zacchia Lun, C. Rinaldi, A. Alrish, A. D'Innocenzo, and F. Santucci, "On the impact of accurate radio link modeling on the performance of WirelessHART control networks," in *Proc. IEEE Conf. Comput. Commun.*, Jul. 2020, pp. 2430–2439.
[76] C. Fischione, F. Graziosi, and F. Santucci, "Approximation for a sum of on-off lognormal processes with wireless applications," *IEEE Trans. Commun.*, vol. 55, no. 10, pp. 1984–1993, Oct. 2007.
[77] C. Liu and F. Li, "Spectrum modelling of OFDM signals for WLAN," *Electron. Lett.*, vol. 40, no. 22, pp. 1431–1432, 2004.
[78] T. van Waterschoot, V. Le Nir, J. Duplicy, and M. Moonen, "Analytical expressions for the power spectral density of CP-OFDM and ZP-OFDM signals," *IEEE Signal Process. Lett.*, vol. 17, no. 4, pp. 371–374, Apr. 2010.
[79] R. López-Valcarce, "General form of the power spectral density of multicarrier signals," *IEEE Commun. Lett.*, vol. 26, no. 8, pp. 1755–1759, Aug. 2022.
[80] X. Liu, J. Guo, G. Bhatti, P. Orlik, and K. Parsons, "Load balanced routing for low power and lossy networks," in *Proc. IEEE Wireless Commun. Netw. Conf. (WCNC)*, Apr. 2013, pp. 2238–2243.
[81] H. A. A. Al-Kashoash, H. Kharrufa, Y. Al-Nidawi, and A. H. Kemp, "Congestion control in wireless sensor and 6LoWPAN networks: Toward the Internet of Things," *Wireless Netw.*, vol. 25, no. 8, pp. 4493–4522, Nov. 2019.
[82] M. B. G. Cloosterman, L. Hetel, N. van de Wouw, W. P. M. H. Heemels, J. Daafouz, and H. Nijmeijer, "Controller synthesis for networked control systems," *Automatica*, vol. 46, no. 10, pp. 1584–1594, Oct. 2010.
[83] G. Ren, Y. Chang, and H. Zhang, "A new SNR's estimator for QPSK modulations in an AWGN channel," *IEEE Trans. Circuits Syst. II, Exp. Briefs*, vol. 52, no. 6, pp. 336–338, Jun. 2005.
[84] D. L. Kreher and D. R. Stinson, *Combinatorial Algorithms: Generation, Enumeration, and Search* (Discrete Mathematics and its Applications). Boca Raton, FL, USA: CRC Press, 2020.

[85] P. Sadeghi, R. Kennedy, P. Rapajic, and R. Shams, "Finite-state Markov modeling of fading channels—A survey of principles and applications," *IEEE Signal Process. Mag.*, vol. 25, no. 5, pp. 57–80, Sep. 2008.
[86] J. P. Hespanha, P. Naghshtabrizi, and Y. Xu, "A survey of recent results in networked control systems," *Proc. IEEE*, vol. 95, no. 1, pp. 138–162, Jan. 2007.
[87] C. De Persis and P. Tesi, "A comparison among deterministic packet-dropouts models in networked control systems," *IEEE Control Syst. Lett.*, vol. 2, no. 1, pp. 109–114, Jan. 2018.
[88] G. Rubino and B. Sericola, "Sojourn times in finite Markov processes," *J. Appl. Probab.*, vol. 26, no. 4, pp. 744–756, Dec. 1989.
[89] M. Z. Q. Chen, L. Zhang, H. Su, and G. Chen, "Stabilizing solution and parameter dependence of modified algebraic Riccati equation with application to discrete-time network synchronization," *IEEE Trans. Autom. Control*, vol. 61, no. 1, pp. 228–233, Jan. 2016.
[90] O. L. V. Costa, M. D. Fragoso, and R. P. Marques, *Discrete-Time Markov Jump Linear Systems*. London, U.K.: Springer, 2005.
[91] J. Apkarian, P. Karam, and M. Lévis, "Inverted pendulum experiment for MATLAB/simulink users," Quanser, Inc, Markham, ON, Canada, Student Workbook, 2012.

YURIY ZACCHIA LUN (Member, IEEE) received the M.S. degree in telecommunications engineering from the University of L'Aquila, L'Aquila, Italy, in 2012, and the joint Ph.D. degree in computer science from the Gran Sasso Science Institute (GSSI), L'Aquila, and the IMT School for Advanced Studies Lucca, Lucca, Italy, in 2017. In 2017, he was a Visiting Ph.D. Student in ERASMUS+ Traineeship with the Department of Computer Science, University of Oxford, U.K. He was a Research Collaborator with the University of L'Aquila and the Center of Excellence DEWS, from 2017 to 2018, and the IMT School for Advanced Studies Lucca, from 2018 to 2022. Since 2022, he has been an Assistant Professor with the Department of Information Engineering, Computer Science and Mathematics (DISIM), Telecommunications Systems and Technologies for Monitoring and Automation Applications Research Group, University of L'Aquila. His research interests include co-designing communication, computation, and control, formal methods, stochastic hybrid systems, wireless networked control systems, and cyber-physical system security.

CLAUDIA RINALDI (Member, IEEE) received the Laurea (cum laude) and Ph.D. degrees in electronic engineering from the University of L'Aquila, Italy, in 2005 and 2009, respectively. Additionally, she holds a master's degree in trumpet and a bachelor's degree in electronic music from the Conservatory of Music of L'Aquila in 2006 and 2013, respectively. She is currently a Researcher with the National Inter-University Consortium for Telecommunications (CNIT) and an Adjunct Professor with the Department of Information Engineering, Computer Science and Mathematics, University of L'Aquila, Italy. She is also involved in the design, modeling, and optimization of communication algorithms, with a particular emphasis on the physical layer and digital signal processing solutions for hardware implementations, especially in relation to digital transparent processors. Her primary research interests include digital signal-processing algorithms and the broader application of technology in artistic fields.

ALESSANDRO D'INNOCENZO (Member, IEEE) received the Laurea degree (cum laude) in electrical engineering and the Ph.D. degree in electrical and information engineering from the University of L'Aquila, Italy, in 2000 and 2007, respectively. He has been a Postdoctoral Researcher with the Department of Electrical and Information Engineering, University of L'Aquila, and the Department of Electrical and Systems Engineering, University of Pennsylvania, USA. Since January 2010, he has been an Assistant Professor with the Department of Information Engineering, Computer Science and Mathematics, University of L'Aquila. He is currently an Associate Professor with the University of L'Aquila. His research interests include networked systems and learning methods for control, with applications in industrial and building automation. He received the Fondazione Filauro Award for Ph.D. Students, in 2005, and the Best Application Paper Award at European Control Conference, in 2015.

FORTUNATO SANTUCCI (Senior Member, IEEE) received the Laurea and Ph.D. degrees in electronic engineering from the University of L'Aquila, L'Aquila, Italy, in 1989 and 1994, respectively. In 1989, he was with Selenia Spazio S.p.A., Rome, Italy. From 1991 to 1992, he held a research fellowship with the Solid State Electronics Institute, National Research Council, Rome. He was a Visiting Researcher with the University of Victoria, Victoria, BC, Canada, and has been involved in visits to several universities worldwide. Since 1994, he has been with the University of L'Aquila, where he is currently a Professor of telecommunications with the Department of Information Engineering, Computer Science and Mathematics. He is also the Deputy Director of the Center of Excellence Ex-EMERGE, University of L'Aquila, with a focus on connected vehicles. He is the Co-Founder of WEST Aquila S.r.l., a spin-off of the University of L'Aquila, and held other management positions with the same university: among those he has been a member of the Academic Senate. He has authored or coauthored more than 250 papers in international journals or conference proceedings. His research interests include energy-efficient communication paradigms for the Internet of Things, vehicular communication networks, network security, and advanced signal processing for satellite transponders and 5G infrastructures. He is a member of the Board of the Radiolabs Consortium. He is a member of several technical committees of the IEEE Communications Society and a member of editorial boards. From 2000 to 2013, he was an Editor of IEEE TRANSACTIONS ON COMMUNICATIONS.

Open Access funding provided by 'Università degli Studi dell'Aquila' within the CRUI CARE Agreement